

# Modeling Nucleation, Growth and Ostwald Ripening in Crystallization Processes: A Comparison Between Population Balance and Kinetic Rate Equation

Thomas Vetter,<sup>†</sup> Martin Iggländ,<sup>†</sup> David R. Ochsenbein,<sup>‡</sup> Flurin S. Hänseler,<sup>†,¶</sup>  
and Marco Mazzotti<sup>\*,†</sup>

*Institute of Process Engineering, ETH Zurich, Sonneggstrasse 3, CH-8092 Zurich, Switzerland, and Automatic Control Laboratory, ETH Zurich, Physikstrasse 3, CH-8092 Zurich, Switzerland*

E-mail: marco.mazzotti@ipe.mavt.ethz.ch

Phone: +41 44 632 2456. Fax: +41 44 632 1141

## Abstract

1  
2 In this work, we investigate a comprehensive model describing nucleation, growth  
3 and Ostwald ripening based on the kinetic rate equation and compare it to commonly  
4 used population balance equation models that either describe nucleation and crystal  
5 growth or crystal growth and Ostwald ripening. The kinetic rate equation gives a  
6 microscopic description of crystallization, i.e., the process is seen as an attachment

---

\*To whom correspondence should be addressed

<sup>†</sup>Institute of Process Engineering, ETH Zurich, Sonneggstrasse 3, CH-8092 Zurich, Switzerland

<sup>‡</sup>Automatic Control Laboratory, ETH Zurich, Physikstrasse 3, CH-8092 Zurich, Switzerland

<sup>¶</sup>Current affiliation: Transport and Mobility Laboratory, EPF Lausanne

7 and detachment of crystals of different sizes to/from each other, thereby changing  
8 their size. A hybrid model is employed in which the discrete kinetic rate equation is  
9 used to describe the smallest particle sizes while a Fokker-Planck equation is used to  
10 approximate the kinetic rate equation at larger particle sizes. This allows us to cover  
11 crystals in a size range starting from a single molecule up to macroscopic particle sizes  
12 and to solve the model numerically with reasonable computational effort and great  
13 accuracy. We show that the model based on the kinetic rate equation describes the  
14 processes of nucleation, crystal growth and Ostwald ripening accurately in a single,  
15 continuous model. This is set in contrast with classical population balance equation  
16 models that require, due to their underlying assumptions, separating the process of  
17 nucleation from the process of Ostwald ripening. We compare the results of the two  
18 models for different sets of parameters (such as different solubilities, surface tensions,  
19 initial supersaturations and seed distributions). Using these results, we assess the  
20 advantages and disadvantages of models based on kinetic rate equation in comparison  
21 to models employing a population balance equation.

## 22 **1 Introduction**

23 In crystallization processes a solute is transferred from a liquid or vapor to a solid phase due  
24 to a difference in chemical potential between the two phases. This process is usually described  
25 as a combination of several mechanisms: the formation of the new phase (nucleation), growth  
26 of crystals and secondary effects such as agglomeration and breakage. The combination  
27 of these effects determines the evolution of the particle size distribution (PSD) until the  
28 supersaturation of the solution is depleted. When starting from an initially solid-free system,  
29 nucleation is dominant at the beginning of the process, when typically the difference in  
30 chemical potential between solution and the solid phase, or supersaturation, is high. Crystal  
31 growth becomes significant as soon as crystals are present in the suspension and will dominate  
32 the decrease of supersaturation after some time. Crystal breakage and agglomeration on the

33 other hand are dominated by particle-particle interactions, reactor design and hydrodynamics  
34 and only have an influence on the size and structure of particles, but do not directly affect  
35 the solution concentration. After the depletion of supersaturation, a mechanism known as  
36 Ostwald ripening<sup>1,2</sup> (also referred to as coarsening, aging, or simply ripening) takes over  
37 and further influences the evolution of the particle size distribution, while breakage and  
38 agglomeration can continue to act on the crystals.

39 Two established classes of models have been frequently used to describe the governing  
40 mechanisms of these processes in detail; the goal of this work is to compare them and to  
41 identify similarities and differences between the two: Population balance equation (PBE)  
42 models<sup>3-5</sup> and models based on the kinetic rate equation (KRE)<sup>6</sup>.

43 PBE models applied to crystallization processes have been widely described in the litera-  
44 ture, accounting for various combinations of the mechanisms described above. The simplest  
45 models describe only growth processes<sup>7,8</sup>. For unseeded crystallizations, nucleation is included  
46 using nucleation rates based on classical nucleation theory<sup>9-12</sup>, typically expressed as functions  
47 of the mechanisms considered (primary or secondary; homogeneous or heterogeneous)<sup>13,14</sup>.  
48 The secondary mechanisms breakage and agglomeration have been the subject of several  
49 works<sup>3,15-19</sup>. The size-dependence of solubility, which governs Ostwald ripening, has been  
50 considered and modeled by several authors<sup>20-25</sup>, as reviewed recently<sup>26</sup>.

51 Though very powerful, PBE models cannot describe Ostwald ripening and nucleation  
52 simultaneously. This is because the nucleation models assume a constant critical size, while  
53 the Ostwald ripening models require the critical size to be a function of the supersaturation.  
54 This situation is unsatisfactory, both conceptually and practically, since the basic mechanisms  
55 behind both nucleation, growth and ripening are the same and in some applications, e.g.,  
56 precipitation of multiple polymorphs,<sup>27</sup> nucleation and growth or ripening occur for different  
57 solid phases at the same time. A model which includes all these steps has been presented by  
58 Kashchiev,<sup>6</sup> based on monomolecular interactions between the solution and the solid phase.  
59 This model has been used to describe nucleation, growth and ripening of silica polymorphs

60 from a geological perspective<sup>27</sup> and in semiconductor nanocrystals.<sup>28</sup> Other models have  
61 been presented which cover all three stages of crystallization, but they suffer from limitations  
62 such as the use of simplified nucleation models,<sup>29–33</sup> or the use of different model equations  
63 for each stage<sup>34–36</sup>.

64 In this work, we will first review the important aspects of the models used (Section 2).  
65 We use dimensionless formulations to identify key parameters in both models (Section 2.3)  
66 and then investigate the influence of these parameters on the kinetics of nucleation, crystal  
67 growth and Ostwald ripening in seeded and unseeded processes at constant and varying  
68 supersaturation (Section 3). Presenting these different types of simulations allows focusing  
69 on each kinetic phenomenon separately, so that the consistency of the PBE and KRE models  
70 can be thoroughly compared and differences and similarities can be highlighted. In the final  
71 part of the results section, simulations in which nucleation, crystal growth and Ostwald  
72 ripening are modeled within a continuous framework (based on the kinetic rate equation)  
73 are presented. We then define characteristic times for nucleation and the start of Ostwald  
74 ripening and their dependence on key model parameters is investigated.

## 75 **2 Modeling of the crystallization process**

76 In the following, we will review the current status of both population balance equation and  
77 kinetic rate equation models in relation to the description of nucleation, growth and ripening.  
78 The aim of this section is not to give the reader a complete overview of the subject, but to  
79 introduce the necessary background and to put our investigation in its proper context.

80 In both models, it is assumed that crystals can be described by a single characteristic  
81 length and that the surface tension between a crystal and its surrounding liquid can be  
82 represented by a single value. Although these are both obvious simplifications for faceted  
83 crystals, we will stick to this description for the sake of simplicity. A volume shape factor  
84 allows to account for different shapes that can be described by one characteristic length, e.g.,

85 cubes, spheres, etc. In this work, we will consider spherical crystals with a characteristic  
 86 diameter and number of molecules  $n$ . For an easier comparison between the two models, we  
 87 use the number of molecules as the size coordinate in both. From a physical point of view  
 88  $n$  assumes integer values only and so it is treated in the KRE model. However, whenever  
 89 convenient, particularly in the PBE model, we treat the number of molecules in a particle as  
 90 a continuous variable called  $\tilde{n}$ .

## 91 2.1 Population balance equation model

92 To model populations of crystals, the population balance equation framework has been used  
 93 extensively<sup>5</sup>. In this paper, we will focus on the interplay of nucleation, crystal growth and  
 94 Ostwald ripening, so that agglomeration and breakage effects are not modeled for simplicity.  
 95 The population balance equation for a well-mixed batch reactor then reads as:

$$\frac{\partial f}{\partial t} + \frac{\partial(vf)}{\partial \tilde{n}} = J\delta(\tilde{n} - \tilde{n}_*) \quad (1)$$

96 where  $f$  is the number density distribution of the crystals in the reactor,  $t$  is the time and  $v$   
 97 is the (size-dependent) rate of crystal growth. By formulating the nucleation term on the  
 98 r.h.s. of Eq. (1) in this way, it is assumed that nuclei appear exclusively at the critical size,  
 99  $\tilde{n}_*$ , with a nucleation rate  $J$  ( $\delta(\tilde{n} - \tilde{n}_*)$  being the Dirac delta function). The assumption  
 100 that nuclei emerge at a single size is made in the vast majority of all publications that use  
 101 population balance equation models and take nucleation into account<sup>37-40</sup>.

102 Supplying appropriate initial and boundary conditions completes the formulation of Eq. (1)  
 103 and allows accounting for seeded crystallization processes. The PBE is coupled with a mass  
 104 balance for the liquid phase, written as

$$\frac{dc}{dt} = -\frac{1}{N_A} \frac{d}{dt} \int_0^{\infty} \tilde{n} f d\tilde{n} \quad (2)$$

105 where  $N_A$  is the Avogadro number. The formulation of Eq. (2) is again completed by an  
 106 appropriate initial condition.

107 Considering how Eq. (1) is formulated, it is clear that sub- and supercritical crystals are  
 108 not treated equally. While the description of supercritical crystals is continuous, crystal nuclei  
 109 appear directly at the critical size, without considering their evolution up to that point, i.e.,  
 110 the “growth” phase of the subcritical crystals is not described. Treating sub- and supercritical  
 111 crystals in this way makes sense if the subcritical size range is small and of lesser interest  
 112 compared to the supercritical size range. Although simplified, many researchers successfully  
 113 use such PBE models to describe crystallization processes where nucleation and/or growth  
 114 occur<sup>11,12,14,18,41–43</sup>. Typically in these cases, solubility is considered to be size-independent  
 115 and the growth rate is defined as proportional to a power of the difference between actual  
 116 concentration and solubility, i.e.,  $v \propto (c - c_\infty)^b$ .

117 However, it is mandatory to accurately describe subcritical crystals when Ostwald ripening  
 118 is considered, because this phenomenon is indeed a consequence of the opposite behavior  
 119 of subcritical crystals, which dissolve, and supercritical crystals, that grow<sup>26</sup>. This is  
 120 accomplished by using a size-dependent growth rate incorporating the Gibbs-Thomson  
 121 relationship<sup>7</sup>. In a general form, such a growth rate can be written as:

$$v(\tilde{n}) = k\tilde{n}^a N_A^b \left( c - c_\infty \exp\left(\frac{\alpha}{\tilde{n}^{1/3}}\right) \right)^b \propto (c - c_*(\tilde{n}))^b \quad (3)$$

122 where  $k$  is a rate constant,  $\alpha$  is the dimensionless capillary length (see Appendix A in the  
 123 supporting information for a derivation),  $a$  and  $b$  are constants which depend on the growth  
 124 mechanism,  $c_\infty$  is the bulk solubility (the solubility of an infinitely large particle) and  $c_*$   
 125 is the size-dependent solubility of a particle of size  $\tilde{n}$ . This expression results in a growth  
 126 rate that is positive for supercritical crystals and negative for subcritical crystals (note that  
 127  $b$  is an odd integer). Eq. (3) can be used to approximate analytically derived expressions  
 128 for different growth rate mechanisms (e.g., diffusion limited growth, 2D nucleation or spiral

129 growth) by changing the parameters  $k$ ,  $a$  and  $b$ .

130 Unfortunately, the growth rate expression in Eq. (3) cannot be reconciled with nucleation  
131 as written in Eq. (1). This is because nuclei formed at a finite critical size consume supersat-  
132 uration (cf. Eq. (2)) which leads to an increase in the critical size (see Appendix A in the  
133 supporting information). As a consequence, nuclei formed at the critical size at one point  
134 in time would start to dissolve immediately thereafter and no stable, supercritical crystals  
135 could ever be formed.

136 One approach to overcome this difficulty is that of allowing the particle size to change  
137 randomly (see e.g. Ramkrishna<sup>5</sup>, Chapter 2.10). This approach involves first describing the  
138 random component of the particle evolution using a stochastic equation, which includes a  
139 term that varies randomly with time with a weight that is a function of time and particle size.  
140 Then this can be incorporated into the PBE using Ito's calculus,<sup>44</sup> thus obtaining a PBE  
141 that contains the same terms as Eq. (1) plus a second order derivative of the particle size  
142 distribution  $f$  multiplied by a time and size dependent coefficient. This last term accounts  
143 for random changes in particle size by introducing a dispersion effect, typical of second order  
144 terms, along the internal coordinate  $\tilde{n}$ . In this way, particles can cross the critical size and  
145 grow beyond it, even when the size-dependent growth and nucleation terms introduced above  
146 alone would not allow for that. A detailed discussion of this approach, which is very rarely  
147 used, is beyond the scope of this work.

148 Another alternative often employed to resolve this inconsistency is to treat the different  
149 phases of the crystallization process using two separate models. When using such an approach,  
150 nucleation and growth are separated from the Ostwald ripening regime by assuming that  
151 nucleation occurs at high supersaturation with a rate that depends on the (varying) super-  
152 saturation and that the solubility in that process phase can be considered size-independent.  
153 The only way to accomplish this and be consistent with the Gibbs-Thomson relationship is if  
154  $\alpha = 0$ , so that the critical size becomes zero and supersaturation-independent as well (see  
155 Appendix A in the Supporting Information)<sup>37</sup>. However, one also finds the use of non-zero

156 (but negligibly small) nuclei sizes in the literature<sup>19,39</sup> and of supersaturation-dependent  
 157 nuclei sizes<sup>38</sup>, which is inconsistent with the Gibbs-Thomson relationship, but often found  
 158 accurate enough for the purposes of these studies.

159 Following classical nucleation theory, the nucleation rate  $J$  is typically described in a form  
 160 similar to

$$J = K_1 S \exp\left(-\frac{K_2}{\ln^2 S}\right) \quad (4)$$

161 where  $S = c/c_\infty$  is the supersaturation,  $K_1$  is a parameter determined by the kinetic aspects  
 162 of nucleation, whose various expressions can be found in the literature<sup>6,45,46</sup>, and  $K_2$  is a  
 163 parameter that depends purely on the thermodynamic properties of the system. According  
 164 to classical nucleation theory, the argument of the exponential function in the last equation  
 165 is proportional to the work to form a crystal of critical size,  $\Delta G(\tilde{n}_*)$ , as given by:

$$\frac{K_2}{\ln^2 S} = \frac{\Delta G(\tilde{n}_*) N_A}{RT} = \frac{\alpha^3}{2 \ln^2 S} \Rightarrow K_2 = \frac{\alpha^3}{2} \quad (5)$$

166 Despite its strong assumptions and its obvious inconsistencies, this simplified model  
 167 delivers a sufficiently accurate description of the crystallization process before Ostwald ripening  
 168 becomes dominant. Note that the time when Ostwald ripening becomes important depends  
 169 on the crystallization kinetics, the size dependence of the solubility, the size distribution of  
 170 the crystals and the supersaturation in the crystallizer (see Iggland and Mazzotti<sup>26</sup> for a  
 171 detailed parameter study). Arriving at an essentially arbitrary threshold supersaturation,  
 172 the population of particles resulting from such a nucleation and crystal growth model is then  
 173 fed to a model describing Ostwald ripening<sup>20,21,26</sup>. In this model, nucleation is assumed  
 174 to be effectively absent due to a low remaining supersaturation (i.e.,  $J = 0$ ), so that the  
 175 discontinuity at the critical size can be removed and the sub- and supercritical crystals can  
 176 be described in a continuous fashion. Hence, in these models the proper description of the  
 177 size-dependence of solubility, the growth rate, and the supersaturation dependency of the  
 178 critical size is restored. However, at which value of supersaturation the switch between

179 the model describing nucleation and the model describing Ostwald ripening is made is not  
180 clearly defined. Therefore, a model that describes all stages (nucleation, growth and Ostwald  
181 ripening) with the same model equations constitutes an appreciable improvement from a  
182 conceptual and practical point of view.

## 183 **2.2 Model based on the kinetic rate equations**

184 The kinetic rate equation model<sup>6</sup> describes particles based on attachment and detachment of  
185 single molecules, or of clusters of molecules, according to the pseudo-reaction scheme



186 Here,  $A_n$  denotes a crystal of size  $n$ ,  $g(n, j)$  is the rate constant of the two-particle attachment  
187 “reaction” of a crystal of size  $n$  to a crystal of size  $j$ , and  $h(n + j, n)$  is the rate constant of the  
188 one-particle detachment of a crystal of size  $j$  from a crystal of size  $n + j$ . It is noteworthy that  
189 the attachment reaction accounts for both crystal growth (when  $n$  or  $j$  is 1) and agglomeration,  
190 whereas the detachment reaction accounts for both dissolution (when  $n$  or  $j$  equals 1) and  
191 breakage. Nucleation is not described explicitly as in the PBE model, but occurs naturally  
192 as a result of the interplay of the ensemble of reactions in Eq. (6), provided attachment and  
193 detachment rates are properly defined.

194 Eq. (6) describes the evolution of sub- and supercritical crystals, accounting for all  
195 mechanisms, in a single model. The importance of this inclusion is evidenced by several  
196 recent findings. To make an example, a study about the formation of platinum nanoparticles  
197 highlighted that agglomeration of subcritical crystals plays an important role in nucleation.<sup>47</sup>  
198 For such cases, models formulated in the spirit of Eq. (6) would provide distinct advantages over  
199 models based on Eq. (1). The goal of the present study, however, is the union of nucleation,  
200 growth and Ostwald ripening; as agglomeration and breakage are not a prerequisite for  
201 nucleation, they are neglected in the following for simplicity. This leaves us with the following

202 equations for the concentration  $Z_n$  of particles of size  $n$  (as originally outlined by Szilard and  
 203 implemented by Farkas<sup>10</sup>):

$$\frac{dZ_1}{dt} = 2h(2)Z_2 + \sum_{j=3}^{\infty} h(j)Z_j - 2g(1)Z_1^2 - Z_1 \sum_{j=2}^{\infty} g(j)Z_j \quad (7a)$$

$$\frac{dZ_n}{dt} = g(n-1)Z_1Z_{n-1} + h(n+1)Z_{n+1} - g(n)Z_1Z_n - h(n)Z_n \quad \text{for } n \geq 2 \quad (7b)$$

204 Note that Kashchiev<sup>6</sup> uses the terminology “master equation” for these deterministic equa-  
 205 tions, i.e., a term that is typically used for similar, but stochastic equations in material and  
 206 electrochemical science (and related fields). In order avoid confusion, we instead use the  
 207 term “kinetic rate equation” throughout this article. Also note that the argument of the  
 208 attachment and detachment rate constants,  $g(n)$  and  $h(n+1)$ , has been simplified to reflect  
 209 that only monomer attachments and detachments are considered.

210 Regarding the functional form of both rates, we follow the treatment by Kashchiev<sup>6</sup>. For  
 211 the attachment rate this yields

$$g(n) = kn^a \quad (8)$$

212 where the values of  $k$  and  $a$  depend on the substance under consideration and on the rate-  
 213 limiting mechanism in the attachment of solute molecules to the crystals. We use a value  
 214 of  $a = 1/3$  unless otherwise stated, which corresponds to attachment controlled by volume  
 215 diffusion (see Kashchiev<sup>6</sup>, pages 141-143). An exemplary value of  $k = 6.86 \times 10^{-18} \text{ m}^3 \text{ s}^{-1}$  is  
 216 chosen for all simulations, which is a realistic choice for a typical organic substance; a derivation  
 217 of these values from readily available substance properties can be found elsewhere<sup>6,46,48</sup>. We  
 218 will show in Section 2.3 that the choice of the  $k$  value can be made without loss of generality.  
 219 Since the attachment rate is obviously proportional to the concentration of crystals containing  
 220 a single molecule, it is implicitly dependent on the supersaturation.

221 The detachment frequency can be derived by letting the frequency of detachment and

222 attachment for a crystal of exactly the critical size,  $n_*$ , be equal, since the driving force for  
 223 either growth or dissolution vanishes at that crystal size<sup>6,48</sup>; therefore:

$$h(n) = g(n)Z_1^*(n) \quad (9)$$

224 where  $Z_1^*(n)$  is the solubility of a crystal of size  $n$ , analogously to  $c_*$ .

225 Clearly, this type of discrete description of particles requires keeping track of a huge  
 226 number of particle sizes if macroscopic particles are to be described. This model can be  
 227 transformed into a continuous form (see for example Kashchiev<sup>6</sup>), in which the discrete  
 228 particle size  $n$  and particle size distribution  $Z_n$  are replaced by their continuous counterparts,  
 229  $\tilde{n}$  and  $\tilde{Z}(\tilde{n})$ :

$$\frac{\partial \tilde{Z}}{\partial t} + \frac{\partial}{\partial \tilde{n}} \left( v \tilde{Z} - \frac{1}{2} \frac{\partial (H \tilde{Z})}{\partial \tilde{n}} \right) = 0 \quad (10)$$

230 where  $v$  and  $H$  are the net growth rate and effective dispersion coefficient, respectively.

231 In this formulation, the net growth rate is given by:

$$v(\tilde{n}) = g(\tilde{n})Z_1 - h(\tilde{n}) \quad (11)$$

232 and the effective dispersion coefficient by:

$$H(\tilde{n}) = g(\tilde{n})Z_1 + h(\tilde{n}) \quad (12)$$

233 Substituting Eqs. (8) and (9) into Eq. (11) yields:

$$v(\tilde{n}) = k\tilde{n}^a \left( Z_1 - Z_{1,\infty} \exp\left(\frac{\alpha}{\tilde{n}^{1/3}}\right) \right) = k\tilde{n}^a N_A \left( c - c_\infty \exp\left(\frac{\alpha}{\tilde{n}^{1/3}}\right) \right) \quad (13)$$

234 Note that this is the same as the equation for the growth rate in the PBE model, Eq. (3),  
 235 provided that the exponent  $b$  in Eq. (3) is chosen to be unity, hence the same symbol  $v(\tilde{n})$   
 236 is used in both equations. The choice of  $b = 1$  is a natural one when the “reactions” in

237 Eq. (6) and the law of mass action are considered. Growth rate expressions that describe  
 238 mechanisms such as birth and spread or spiral growth (see for example Ohara and Reid  
 239 <sup>49</sup>) exhibit a different concentration dependence and could be modeled by adjusting the  
 240 underlying reaction scheme. It is evident that different mechanisms could be rate controlling  
 241 for different sizes of crystals, however, in order to not further complicate matters, we consider  
 242 attachment and detachment kinetics to be controlled by volume diffusion over the whole size  
 243 range.

244 The continuous formulation, which is derived from a Taylor expansion, introduces an  
 245 error, particularly for small particles. Ozkan et al.<sup>27</sup> proposed to combine the advantages of  
 246 both the discrete and continuous formulations by using a hybrid model. The idea behind this  
 247 approach is illustrated in Figure 1. Up to a size  $N$ , the discrete formulation is used, and the  
 248 continuous formulation is used for larger particles (in this work,  $N = 50$ ). At the boundary  
 249 between the two parts of the size domain, conservation of flux is enforced. The reader is  
 250 referred to Appendix C in the supporting information, where the flux conservation and the  
 numerical scheme to solve the Fokker-Planck equation are reported in detail.

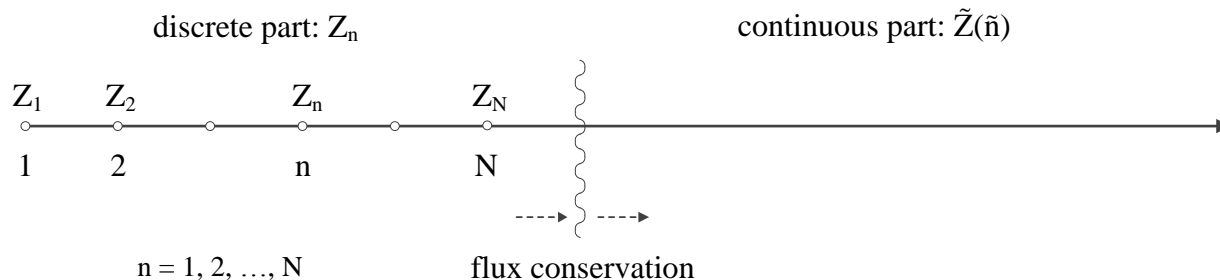


Figure 1: Combination of discrete and continuous descriptions of the crystal size domain. The two parts are connected at size  $N + 1$ . Details can be found in Appendix C of the supporting information.

251

252 Finally, it is worth noting that the continuous formulation of the KRE consists of an  
 253 equation (Eq. (10)) that contains a second order derivative of the PSD like the formulation  
 254 of the PBE accounting for random changes of the particle state (see Section 2.1). Contrary  
 255 to the mentioned PBE the function  $H$  constituting the weight of the second order term in

Eq. (10) has a deterministic origin rather than a stochastic one.

### 2.3 Dimensionless formulation of the KRE and the PBE model

The model equations Eqs. (1), (2), (7) and (10) can be made dimensionless by introducing the quantities

$$Y_n = \frac{Z_n}{Z_{1,\infty}} \quad (14)$$

$$\tau = \frac{t}{t_0} \quad (15)$$

where  $t_0$  is a reference time. The reference time is chosen to be:

$$t_0 = (kZ_{1,\infty})^{-1} \quad (16)$$

These dimensionless variables are used to define dimensionless versions of the PBE as well as the discrete and continuous versions of the KRE (see Appendix B in the supporting information for details). For the PBE a dimensionless nucleation rate  $\bar{\phi}$  can be defined, given by

$$\bar{\phi} = \frac{Jt_0}{Z_{1,\infty}} \quad (17)$$

Substituting Eq. (4) and taking the logarithm of both sides yields:

$$\ln\left(\frac{\bar{\phi}}{S}\right) = \ln\left(\frac{t_0 K_1}{Z_{1,\infty}}\right) - \frac{K_2}{\ln^2 S} \quad (18)$$

Let us summarize the model parameters needed to carry out simulations with the KRE and the PBE models. The KRE model depends on only four parameters, namely the nominal solubility  $Z_{1,\infty} = c_\infty N_A$ , the attachment rate constant,  $k$ , both combined in  $t_0$  as in Eq. (16), the constant exponent  $a$  (Eq. (8)) and the constant  $\alpha$ , related to the capillary length (see Eq. 3 in the Appendix). Introducing the dimensionless variables therefore allowed us to discover

269 the scaling dependence between  $k$  and  $Z_{1,\infty}$ . For the PBE model two more parameters are  
270 needed:  $K_1$  and  $K_2$ , though  $K_2$  was already shown to be proportional to  $\alpha^3$  (Eq. (5)) and  
271  $K_1$  will be shown to be a function of  $\alpha$ ,  $k$  and  $Z_{1,\infty}$  in Section 3.1.

## 272 **3 Results**

273 In order to compare the classical PBE model and the KRE model during different phases  
274 of a crystallization process (nucleation, crystal growth and Ostwald ripening) we report  
275 simulations carried out using different parameter sets, thus investigating the influence of the  
276 dimensionless capillary length  $\alpha$  and of the initial supersaturation as well as the effect of the  
277 presence of an initial population of crystals (seeded crystallization). To accomplish this, two  
278 different types of simulations are presented. In the first type of simulations (Section 3.1),  
279 the supersaturation (and therefore the critical size) is kept constant. This has the advantage  
280 that Ostwald ripening is effectively avoided, thus allowing to focus on the mechanisms of  
281 nucleation and crystal growth using simulations of unseeded and seeded processes, respectively.  
282 In the second type of simulation (Section 3.2) we allow the supersaturation to vary during  
283 crystallization, thus permitting the investigation of Ostwald ripening. To this end, we report  
284 simulations of seeded processes starting from a saturated solution. Finally, simulations of  
285 unseeded processes at varying supersaturation are presented. In these last simulations, crystals  
286 are first nucleated, then grown and finally subjected to Ostwald ripening. As explained in  
287 the introductory part of this work, such simulations cannot be carried out in a continuous  
288 fashion using a single, classical PBE model, but are unique of the KRE model.

289 In all the simulations the kinetic rate equation model in its dimensionless form is solved  
290 numerically using the multi-scale approach presented in Section 2.2. While the ordinary  
291 differential equations in the discrete part of the model can easily be solved by standard  
292 integration techniques (in our case we use MATLAB's `ode15s`<sup>50,51</sup>; a multistep solver tailored  
293 explicitly to solving stiff problems), the Fokker-Planck equation in the continuous part of

294 the model is solved using a discretization scheme first proposed by Chang and Cooper<sup>52</sup>,  
 295 which has already been applied to model the nucleation and growth of nanocrystals<sup>28,53</sup>. The  
 296 discretized equations are then again solved with ode15s. We report the detailed procedure  
 297 in the supporting information (Appendix C). Solutions of the classical PBE model in its  
 298 dimensionless form are reported for simulations at constant supersaturation. In these cases  
 299 the solution can be calculated analytically using the method of characteristics<sup>54</sup>.

### 300 **3.1 Simulations at constant supersaturation**

#### 301 **3.1.1 Simulations of unseeded processes: nucleation**

302 Simulations of unseeded processes at constant supersaturation are ideally suited to investigate  
 303 nucleation since many transient phenomena, caused by a varying supersaturation, are elimi-  
 304 nated. Keeping supersaturation constant therefore allows the investigation of a limiting case  
 305 and is useful particularly from a conceptual point of view. An example of the simulation of  
 306 such a case is shown in Figure 2 where the solution of the KRE model is shown as a contour  
 307 plot, i.e., the contour lines indicate level sets of  $\tilde{Y}(\tau, \tilde{n})$ . Note that the color scale used in  
 308 this and the following contour plots is logarithmic and the same for all figures. Analyzing  
 309 the evolution of the PSD shown in this plot, one sees that, in the KRE model, supercritical  
 310 crystals appear only after some delay. This behavior is different from the classical PBE  
 311 model, where constant supersaturation implies an immediate, linear increase in the number  
 312 of crystals over time. In the KRE model, the instantaneous, dimensionless nucleation rate,  $\phi$ ,  
 313 can be calculated from the time derivative of the number of supercritical crystals

$$\phi = \frac{d}{d\tau} \left( \sum_{i=\lceil \tilde{n}_* \rceil}^N Y_n + \int_{\max\{\tilde{n}_*, N+1\}}^{\infty} \tilde{Y} d\tilde{n} \right) \quad (19)$$

314 As previously emphasized, in the KRE model nucleation appears naturally from the interplay  
 315 of attachment and detachment rates without the need of an additional kinetic expression or  
 316 parameters. In contrast, in the PBE model a rate expression specific to nucleation (Eq. (4))

317 is required, and the two additional model parameters  $K_1$  and  $K_2$  have to be assigned. The  
 318 evolution of the number of supercritical crystals for the simulation illustrated in Figure 2 is  
 319 shown in Figure 3, where the nucleation rate is shown to approach a constant value for the  
 320 KRE model after an initial “lag time”. Since the instantaneous dimensionless nucleation rate,  
 321  $\phi(\tau)$ , approaches the stationary value of the nucleation rate,  $\bar{\phi}$ , rather slowly, we define the  
 322 lag time,  $\tau_{\text{lag}}$ , as the time when the relative difference of the instantaneous and stationary  
 323 dimensionless nucleation rate becomes smaller than a threshold:

$$\frac{\phi(\tau_{\text{lag}}) - \bar{\phi}}{\bar{\phi}} \leq \epsilon_{\text{threshold}} \quad (20)$$

324 where the threshold was selected to be  $\epsilon_{\text{threshold}} = 10^{-4}$ . In the simulations reported in this  
 325 work (cf. Table 1) we observed a maximal dimensionless lag time  $\tau_{\text{lag}} \approx 10^3$ . The values of  
 326 the stationary dimensionless nucleation rate can be determined either by evaluating  $\phi$  at  
 327 large times ( $\tau > 10^6$ ) or by calculating the flux between neighboring points in the discrete  
 328 distribution under steady state conditions

$$\bar{\phi} = \eta_n S X_n - \xi_{n+1} X_{n+1} \quad (21)$$

329 where  $X_n$  indicates the (dimensionless) steady state distribution, which can be approximated  
 330 from  $Y_n$  at large  $\tau$ , and  $\eta_n$  and  $\xi_{n+1}$  are dimensionless attachment and detachment rate  
 331 constants (see Appendix B in the supporting information). It is noteworthy that the shape  
 332 of the stationary crystal size distribution depends on the value of  $a$  in the dimensionless  
 333 attachment and detachment rate constants. To illustrate this, simulations for  $a$  values of  
 334  $[1/3, 4/9, 5/9, 2/3]$  were performed, whose stationary crystal size distributions are reported  
 335 in Figure 4. The change in the stationary distribution is counterbalanced by the change in  
 336 the dimensionless attachment and detachment rates,  $\eta_n S$  and  $\xi_n$ , so that the values obtained  
 337 for  $\bar{\phi}$  are the same, regardless of the value of  $a$ .

338 Using the stationary nucleation rate determined from the above analysis, the KRE model

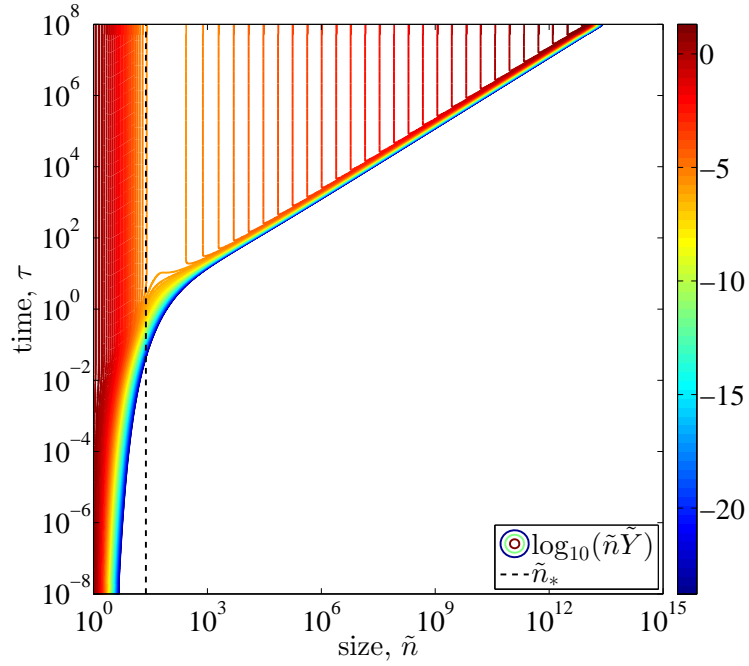


Figure 2: Unseeded simulations at constant supersaturation: Contour plot of the evolution of the volume weighted PSD,  $\tilde{n}\tilde{Y}$ , obtained by solving the multi-scale model based on the kinetic rate equation (note that the color scale is logarithmic). The data represented in this figure stem from a simulation with a supersaturation  $S = 8$  and a dimensionless capillary length  $\alpha = 6$ .

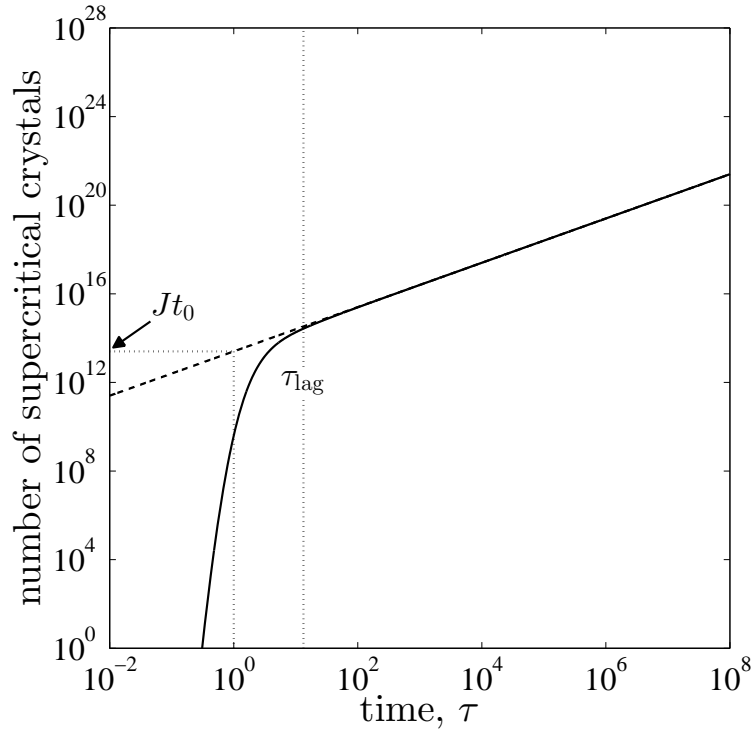


Figure 3: Unseeded simulations at constant supersaturation: evolution of the number of supercritical crystals (simulation at supersaturation  $S = 8$  and a dimensionless capillary length  $\alpha = 6$ ) for the KRE model (solid line) and the classical PBE model (dashed line). The lag time,  $\tau_{\text{lag}}$ , as defined in Eq. (20), is visualized with a dotted line. In this plot the steady state nucleation rate for both models is marked with an arrow on the ordinate.

339 output can be compared to the (analytical) solution of the PBE model with an identical  
 340 nucleation rate. The result is given in Figure 5, where the PSD is shown at different  
 341 times during the process. While the solutions of the two models show similarities, several  
 342 differences can be identified: first, as already outlined, the KRE model describes both sub-  
 343 and supercritical crystals, while the PBE model only accounts for supercritical crystals;  
 344 second, the PSDs obtained from the KRE model have a “front” that is not as sharp as the  
 345 ones obtained by the PBE model. Comparing the PBE (Eq. (1)) and the continuous version  
 346 of the KRE (the Fokker-Planck equation, Eq. (10)), it is clear that the second order term in  
 347 the Fokker-Planck equation causes the unsharp front. However, one should be aware that  
 348 the Fokker-Planck equation is merely a consequence of the Taylor expansion applied to the  
 349 discrete kinetic rate equation (Eq. (7)) in order to arrive at a continuous equation. Hänggi  
 350 et al.<sup>55</sup>, Shizgal and Barrett<sup>56</sup> and Wu<sup>57</sup> provide an extensive overview of alternative ways  
 351 to arrive at a continuous equation and discuss their accuracy (with respect to describing  
 352 the discrete KRE). However, none of these alternatives is equivalent to the PBE, which is  
 353 not surprising, as the description of nucleation in the two models is quite different, i.e., the  
 354 direct formation of a crystal of critical size in the PBE vs. the growth of sub- to supercritical  
 355 crystals in the KRE. It is noteworthy that the unsharp fronts seen in the KRE model are  
 356 *not* merely a result of numerical dispersion, which we have kept insignificant by using a  
 357 discretization grid with geometrical spacing and a fine resolution (see Appendix C in the  
 358 Supporting Information for details).

359 Overall, the solutions of the two models for the simulation presented in Figure 5 are  
 360 remarkably similar despite the different assumptions made in their derivation. To analyze  
 361 the dependence of the stationary nucleation rate on the supersaturation and the capillary  
 362 length the simulations listed in Table 1 have been performed ( $a = 1/3$  for all simulations in  
 363 this table and all subsequently presented simulations).

364 The stationary nucleation rates from these simulations, together with the classical nu-  
 365 cleation rate equation Eq. (18) can be used to find parameter pairs of  $K_1$  and  $K_2$  at given

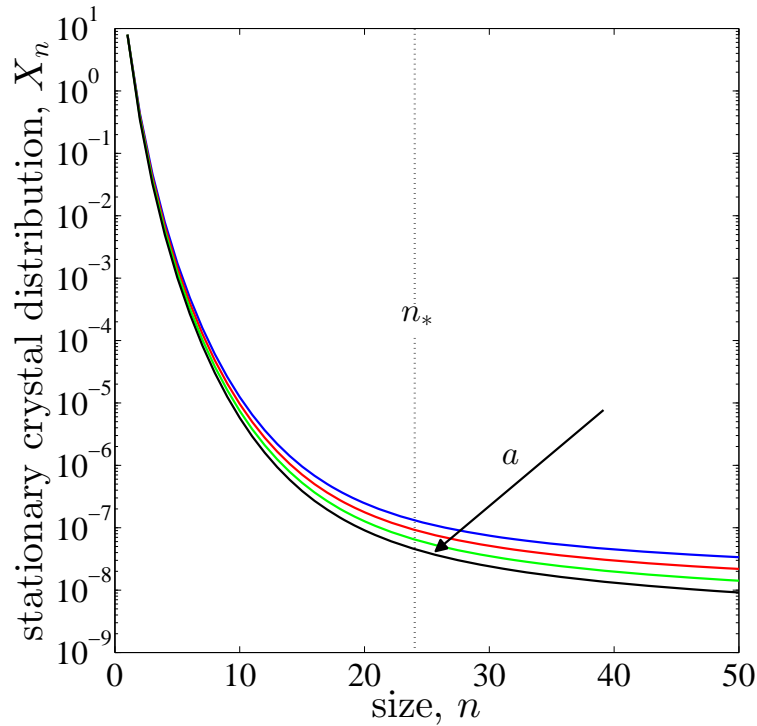


Figure 4: Unseeded simulations at constant supersaturation: Stationary crystal size distributions obtained at small crystal sizes for different values of the exponent  $a$ . The values of  $a$  are  $[1/3, 4/9, 5/9, 2/3]$ . The simulations have been performed with a supersaturation  $S = 8$  and a dimensionless capillary length  $\alpha = 6$ . The critical size,  $n_*$ , is indicated by the dashed line.

Table 1: Overview of unseeded simulations at constant supersaturation

ID	$\alpha$	$S$
CU1a-e	1	1.5–2.5
CU2a-l	2	1.5–6
CU3a-p	3	1.75–16
CU4a-p	4	2.25–20
CU5a-n	5	3–20
CU6a-l	6	4–20
CU7a-j	7	5–20
CU8a-g	8	8–20
CU9a-f	9	10–20
CU10a-d	10	14–20

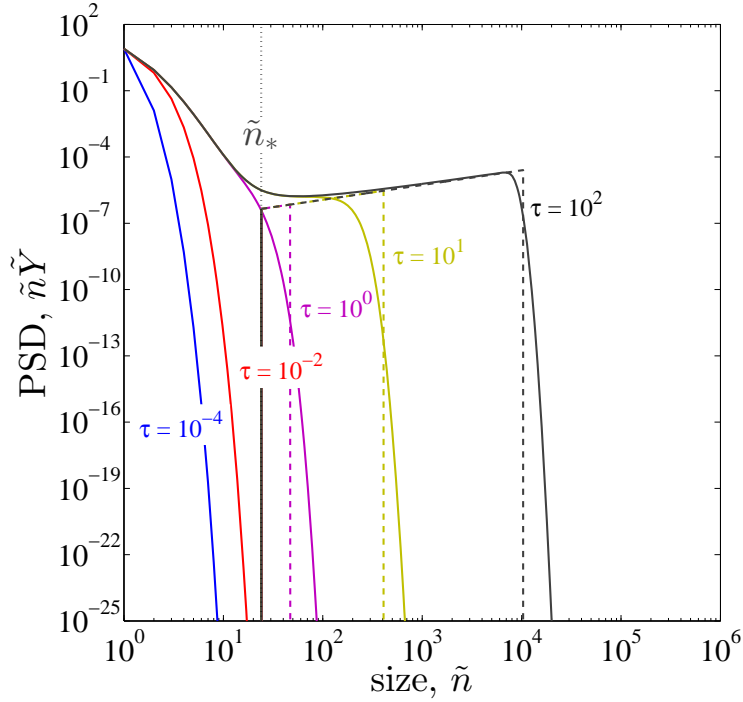


Figure 5: Unseeded simulations at constant supersaturation: Comparison of the results of the classical PBE (dashed lines) to the results of the model based on the kinetic rate equation (solid lines). The different colors represent the PSD at different times. It should be noted that the PSDs for the classical PBE model partially overlap, so that only the vertical/near-vertical “front” is clearly visible for all different times for both models. The data represented in this figure stem from a simulation with a supersaturation  $S = 8$  and a dimensionless capillary length  $\alpha = 6$ .

capillary lengths, as shown in Figure 6.

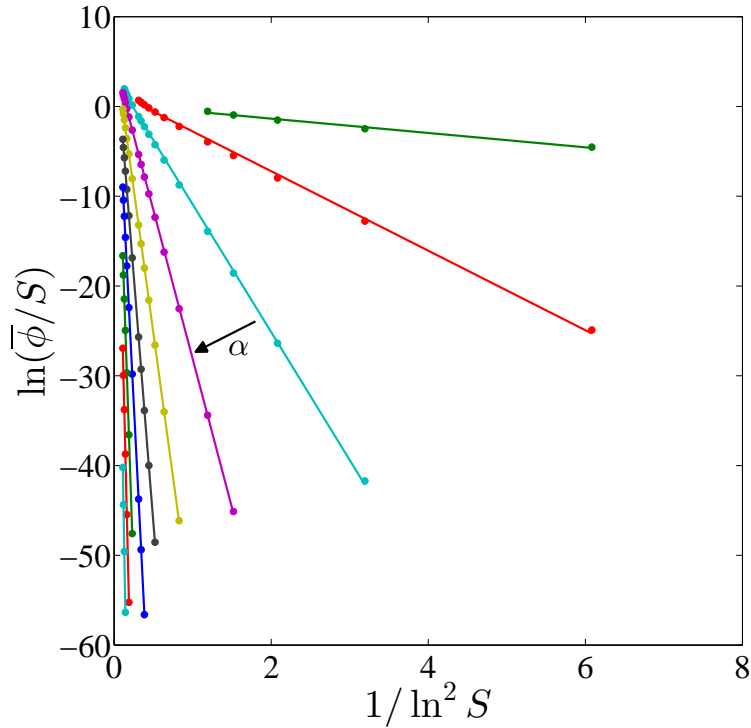


Figure 6: Unseeded simulations at constant supersaturation: linearization of the stationary nucleation rates obtained with the KRE model. The symbols represent the simulated values while the lines represent the linear regressions on these sets of data points. For a list of simulations shown in this figure refer to Table 1.

366

367 In Figure 7,  $\ln(t_0 K_1/Z_{1,\infty})$  and  $K_2$  are plotted as functions of  $\alpha$  and  $\alpha^3$ , respectively. For  
 368 the specific functional form of attachment and detachment rates chosen in this work (Eqs. (8)  
 369 and (9)), these plots show that there is a clear dependence of the ordinate values on  $\alpha$ , i.e.,  
 370 one can see in Figure 7(a) that our simulation data is consistent with the relationship for  
 371  $K_2$  derived earlier, i.e.,  $K_2 = \alpha^3/2$ . Similarly, in Figure 7(b) one sees that the dependence of  
 372  $\ln(t_0 K_1/Z_{1,\infty})$  on  $\alpha$  can be described by an affine function. Explicitly, this function is

$$\ln(t_0 K_1/Z_{1,\infty}) = 1.74 \alpha - 1.79 \quad (22)$$

373 The coefficient of determination by Eq. (22) is  $R^2 = 0.9993$ . This means that as soon as the  
 374 value of  $\alpha$  is known and the attachment and detachment rates are defined, the corresponding

375 values of  $K_1$  and  $K_2$  follow. This indicates that, under the given conditions,  $K_1$  and  $K_2$   
376 introduced in classical nucleation theory are not independent parameters as normally assumed  
377 in classical population balance equation models.

378 Testing the above postulated dependence of  $\ln(t_0 K_1 / Z_{1,\infty})$  on  $\alpha$  against experimental  
379 observations would be an attractive and necessary task. However, such a validation is made  
380 practically impossible by the following two considerations about our model assumptions as  
381 compared to the operating conditions of laboratory experiments:

- 382 • In solution crystallization the supersaturation is often generated either by cooling or  
383 by anti-solvent addition. Both techniques affect the surface tension and therefore the  
384 dimensionless parameter  $\alpha$  in an *a priori* unknown way, thus making the interpretation  
385 of the nucleation rates reported in the literature in the context of our model exceedingly  
386 hard.
- 387 • The crystal growth rate is frequently measured with large crystals that are orders of  
388 magnitude larger than critical nuclei. These measured growth rates are unlikely to  
389 apply to very small crystals.

390 To the best of our knowledge, there is no dataset for a single compound crystallized from  
391 solution that is not affected by these considerations, so that the validation of our simulation  
392 results against experimental data cannot (yet) be carried out. Therefore, the above-mentioned  
393 dependence of  $\ln(t_0 K_1 / Z_{1,\infty})$  on  $\alpha$  simply remains a property that we observed by performing  
394 thorough and comprehensive simulations with the KRE model.

### 395 **3.1.2 Simulations of seeded processes: crystal growth**

396 We now focus our attention on the description of crystal growth at constant supersaturation  
397 in the PBE and KRE model. To this end, a series of seeded simulations is performed where  
398 the seed distributions considered are normal distributions with mean at  $\bar{n}_0$  and standard  
399 deviation of  $\sigma_0$ , as reported in Table 2. To correctly focus on the mechanism of growth only,

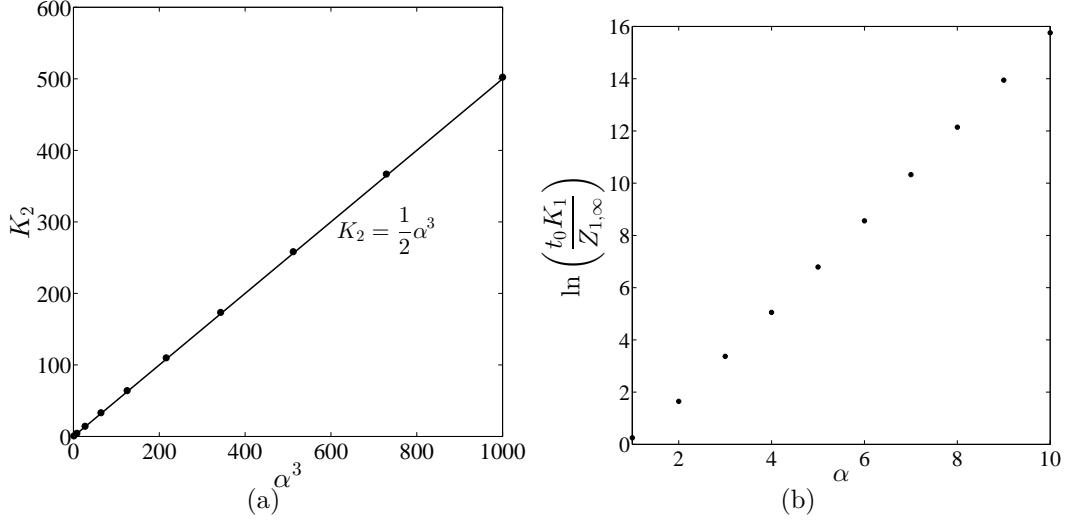


Figure 7: Unseeded simulations at constant supersaturation: (a) dependency of  $K_2$  on  $\alpha^3$ , (b) dependency of  $\ln(t_0 K_1/Z_{1,\infty})$  on  $\alpha$ . The values of  $K_1$  and  $K_2$  have been obtained from the linearizations of the nucleation rates reported in Figure 6 which in turn have been determined from the simulations reported in Table 1.

Table 2: Overview of seeded simulations at constant supersaturation

ID	$\alpha$	$\bar{n}_0$	$\sigma_0$	$S$	$\psi$
CS1a-d	1	$1 \times 10^7$	$5 \times 10^7$	{1.1, 1.4, 1.7, 2}	0.05
CS2a-d	5	$1 \times 10^7$	$5 \times 10^5$	{1.1, 1.4, 1.7, 2}	0.05
CS3a-d	10	$1 \times 10^7$	$5 \times 10^5$	{1.1, 1.4, 1.7, 2}	0.05
CS4a-d	1	$1 \times 10^{10}$	$5 \times 10^8$	{1.1, 1.4, 1.7, 2}	0.05
CS5a-d	5	$1 \times 10^{10}$	$5 \times 10^8$	{1.1, 1.4, 1.7, 2}	0.05
CS6a-d	10	$1 \times 10^{10}$	$5 \times 10^8$	{1.1, 1.4, 1.7, 2}	0.05
CS7a-d	1	$1 \times 10^{13}$	$5 \times 10^{11}$	{1.1, 1.4, 1.7, 2}	0.05
CS8a-d	5	$1 \times 10^{13}$	$5 \times 10^{11}$	{1.1, 1.4, 1.7, 2}	0.05
CS9a-d	10	$1 \times 10^{13}$	$5 \times 10^{11}$	{1.1, 1.4, 1.7, 2}	0.05

400 nucleation is artificially deactivated in both the PBE and KRE model. In the case of the PBE  
 401 model, this is achieved by setting  $\bar{\phi} = 0$ , while in the case of the KRE model nucleation is  
 402 removed by setting the flux from  $n = 1$  to  $n = 2$  to zero. The amount of seed particles added  
 403 to each simulation is defined by the initial holdup ratio  $\psi$ , defined as the ratio between the  
 404 number of molecules initially present in the solid phase to the number of molecules initially  
 405 in the liquid phase:

$$\psi = \frac{\mu_1(\tau = 0)}{S_0} \quad (23)$$

406 where  $S_0$  is the initial supersaturation and  $\mu_1(\tau = 0)$  is the first moment of the initial  
 407 distribution. The dimensionless moments are thereby given by

$$\mu_j = \int_0^{\infty} \tilde{n}^j \tilde{Y} d\tilde{n} \quad (24)$$

408 for the PBE model, and as:

$$\mu_j = \sum_{n=2}^N n^j Y_n + \int_{N+1}^{\infty} \tilde{n}^j \tilde{Y} d\tilde{n} \quad (25)$$

409 for the hybrid kinetic rate equation model.

410 Solving the PBE and KRE model for the cases reported in Table 2, one obtains the  
 411 evolution of the PSD over time. An example of such an evolution for both models (simulation  
 412 CS5c in Table 2) is shown in Figure 8, where the volume weighted PSD is plotted for both  
 413 models at specific values of the dimensionless time. One immediately sees that the PSD  
 414 in the two models evolves similarly, i.e., the mode of the distribution behaves the same in  
 415 both models. However, the width behaves differently. In the case of the KRE model, we  
 416 clearly see a broadening of the PSD over time, while the width of the PSD decreases in the  
 417 PBE model, as one would expect using the growth rate defined in Eq. (13). Similar to the  
 418 nucleation simulation presented in Figure 5, where the “front” of the PSD was observed to  
 419 be less sharp for the KRE model than for the PBE model, the widening of the PSD is again  
 420 a direct consequence of the second order term in the Fokker-Planck equation.

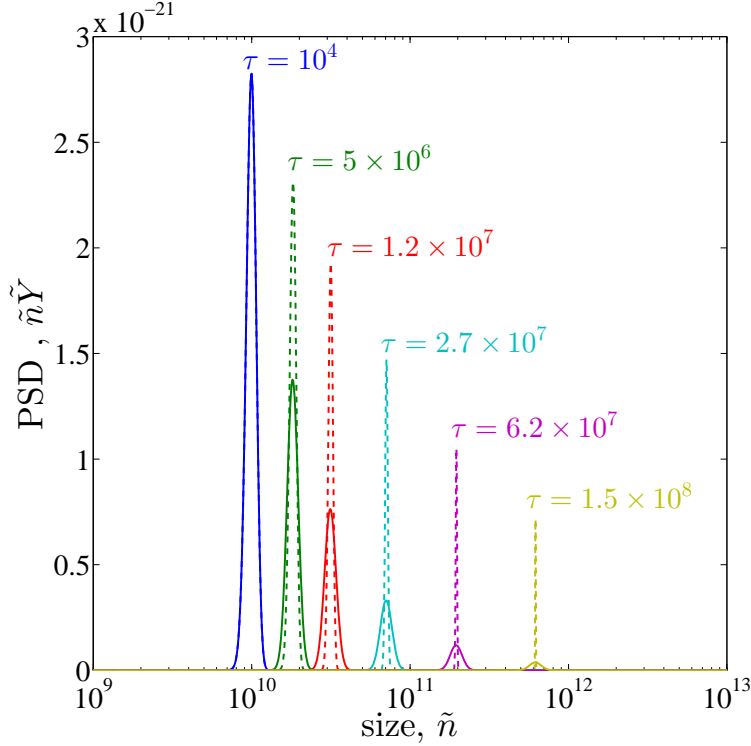


Figure 8: Seeded simulations at constant supersaturation: particle size distribution at selected time points for the KRE model (solid lines) and the PBE model (dashed lines).

421 In order to quantify the effects of varying  $\alpha$ ,  $S$  and seed distribution, we define the volume  
 422 weighted mean size of the particles in the PSD as

$$\bar{n} = \frac{\mu_2}{\mu_1} \quad (26)$$

423 The evolution of the mean size for exemplary simulations for both the KRE and PBE model  
 424 is shown in Figure 9. Focusing on the PBE model (black lines), the evolution of the mean  
 425 size follows the dependency of the growth rate (Eqs. (3) and (13)) on the varied parameters,  
 426 i.e., an earlier increase of the mean size is observed at higher supersaturations (Figure 9(a)),  
 427 lower  $\alpha$  values (Figure 9(b)) and smaller initial particle sizes (Figure 9(c)). One can see  
 428 from all three subfigures that the mean size evolves identically in both models for all sets of  
 429 parameters, so that one can conclude that the KRE models and the PBE models agree well  
 430 in their description of crystal growth.

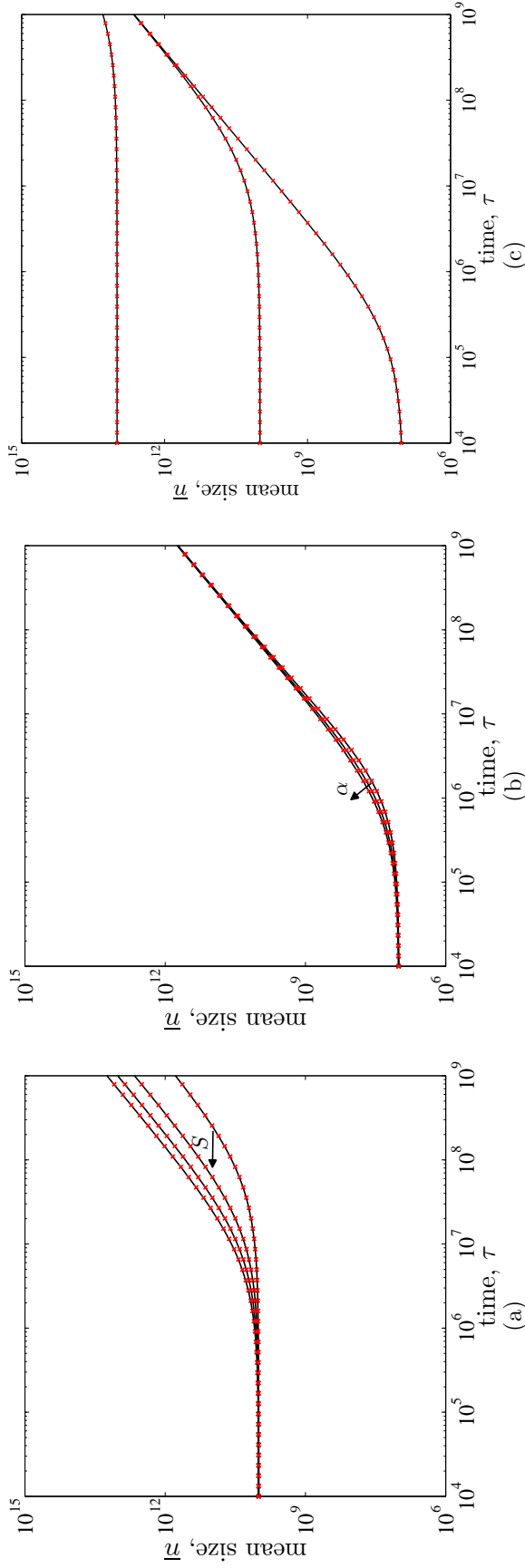


Figure 9: Seeded simulations at constant supersaturation: effect of changing parameters on the evolution of the mean size,  $\bar{n}$ , in the PBE (crosses) and KRE (lines) models. (a) effect of different levels of supersaturation (simulations CS5a-d in Table 2), (b) effect of the dimensionless capillary length  $\alpha$ . (simulations CS1a, CS2a and CS3a in Table 2), (c) effect of different initial particle sizes (simulations CS2c, CS5c and CS8c in Table 2).

## 431 **3.2 Simulations at varying supersaturation**

### 432 **3.2.1 Simulations of seeded processes: Ostwald ripening**

433 Let us now shift our attention from nucleation and growth to Ostwald ripening in this section.  
434 To investigate this mechanism, it is necessary to let the supersaturation vary over time,  
435 i.e., we relax the constant supersaturation assumption of the previous section. Ostwald  
436 ripening is a phenomenon that has been investigated using a plethora of models. Iggland  
437 and Mazzotti<sup>26</sup> recently published an overview of these models and used a full PBE model  
438 to simulate and analyze Ostwald ripening. In this work, we compare simulations using the  
439 KRE model to simulations with the PBE model, while keeping the same parameters in both  
440 models. To this end, we report a series of simulations starting from a saturated solution that  
441 contain different-sized particles, for which the values of the relevant parameters are reported  
442 in Table 3.

443 The complete evolution of the volume weighted PSD calculated using the KRE model for  
444 increasingly large seed distributions (see Table 3) is reported in the form of contour plots in  
445 Figure 10 (note that the seeds are normally distributed in  $\tilde{Y}$  while  $\tilde{n}\tilde{Y}$  is plotted). In the  
446 same plot, we compare the volume-weighted mean particle size (red lines) and critical size  
447 (black lines) obtained using the two models. For all simulations, the critical size lies initially  
448 outside the investigated size region (since we start from a saturated solution the critical size  
449 is infinitely large); it is only after a certain time period that it enters the observed size region.  
450 This decrease in critical size is due to a rise in supersaturation, which in turn is caused by  
451 a net dissolution of particles. As larger particles take considerably longer to fully dissolve,  
452 this delay is an increasing function of seed size, which is in accordance with experimental  
453 observations where Ostwald ripening is effectively negligible for sufficiently large particles.

454 Eventually, the critical size is small enough as to make a sizeable fraction of the particles  
455 become supercritical. This has an impact on the distribution as now the dissolution of crystals  
456 is additionally enhanced by the consumption of solute by the largest particles. This system of

Table 3: Overview of seeded simulations at varying supersaturation

ID	$\alpha$	$S_0$	$\bar{n}_0$	$\sigma_0$	$\psi$
VS1	5	1	$1.5625 \times 10^7$	$1 \times 10^8$	1.5
VS2	5	1	$1.25 \times 10^8$	$1 \times 10^8$	1.5
VS3	5	1	$1 \times 10^9$	$1 \times 10^8$	1.5
VS4	5	1	$3.375 \times 10^9$	$1 \times 10^8$	1.5
VS5	5	1	$8 \times 10^9$	$1 \times 10^8$	1.5
VS6	5	1	$1.5625 \times 10^{10}$	$1 \times 10^8$	1.5

457 simultaneous dissolution and growth may remain in a fragile balance for awhile, as indicated  
 458 by the constant critical size in some plots, particularly for larger seed crystals. Ultimately,  
 459 however, the average size starts to increase and a net decrease of supersaturation can be  
 460 observed with the critical size now trailing the mean size of the particles, both fingerprints of  
 461 Ostwald ripening.

462 Focusing on the contour lines given by the solution of the KRE model it can be seen that,  
 463 immediately at the beginning, small sized clusters are formed in all simulations. Also, the  
 464 rearrangement of the PSD due to dissolution of subcritical particles is evident.

465 The effect of this dissolution on the PSD in different simulations is also visible in Figure 11,  
 466 where volume weighted PSDs at specific points in time are reported. Since almost no change  
 467 in the PSD can be observed for the large seed particles (simulations VS5 and VS6), these  
 468 simulations are omitted from the analysis. Again, the outlined behavior can be observed:  
 469 the change in the PSD starts by dissolving particles while the mode of the PSD remains  
 470 quasi-stationary. When sufficient crystals are dissolved, the remaining particles begin to  
 471 increase in size, which can be seen by the modes of the PSDs shifting to larger sizes.

472 We additionally report two important integral quantities obtained from the simulations in  
 473 Figure 12: the evolution of supersaturation and the evolution of the number of supercritical  
 474 particles. The evolution of supersaturation, cf. Figure 12(a), exhibits a peculiar behavior  
 475 as it indicates that the initially saturated solution becomes undersaturated at early times  
 476 of the simulation. This effect is considered purely kinetic, since the formation of unstable  
 477 oligomers is kinetically favored in comparison to single solute molecules and, since we defined

478 the supersaturation purely on the basis of the single solute molecules ( $Y_1$ ), this causes the  
479 supersaturation to decrease. Hence, this mathematical artifact is unlikely to be observed in  
480 reality (i.e., experimentally). However, the evolution of the supersaturation at later stages is  
481 consistent with LSW theory, i.e., the peak in supersaturation occurs slightly earlier and is  
482 higher for smaller seed particles than for larger ones. Focusing now on the evolution of the  
483 number of supercritical crystals (cf. Figure 12(a)) we notice that the number of supercritical  
484 particles initially increases, which is caused by the fact that the critical size is infinitely  
485 large at the beginning. It has to be stressed that this increase in the number of supercritical  
486 crystals is *not* associated to nucleation, as can be clearly seen from the evolution of the PSDs  
487 in Figures 10 and 11. However, we observe again a consistent behavior at later stages of the  
488 simulations, i.e., the rate of disappearance of supercritical crystals becomes the same for all  
489 the simulations.

490 The outlined behavior is the same in the PBE model of Ostwald ripening<sup>26</sup>, and is also  
491 predicted by the LSW theory<sup>20,21</sup>. In the asymptotic growth stage, the change in the mean  
492 particle size (solid red line for the KRE model; dashed red line for the PBE model) and  
493 critical size (solid black line for the KRE model; dashed black line for the PBE model) is  
494 the same in both models. The behavior in the early stages of the simulation is slightly  
495 different, especially in the simulations with small seed particles. This difference is caused  
496 by the clusters, whose generation at the very beginning of the simulations interferes with  
497 the seed particles, thereby affecting the evolution of the system. Comparing the two models,  
498 one observes that the KRE model predicts a quantitatively comparable behavior to the PBE  
499 model, with differences caused by the presence of clusters.

### 500 **3.2.2 Simulations of unseeded processes: nucleation, crystal growth and Ost-** 501 **wald ripening**

502 The real strength of the KRE model becomes apparent when unseeded simulations starting  
503 from a supersaturated solution are investigated. In these simulations crystals nucleate and

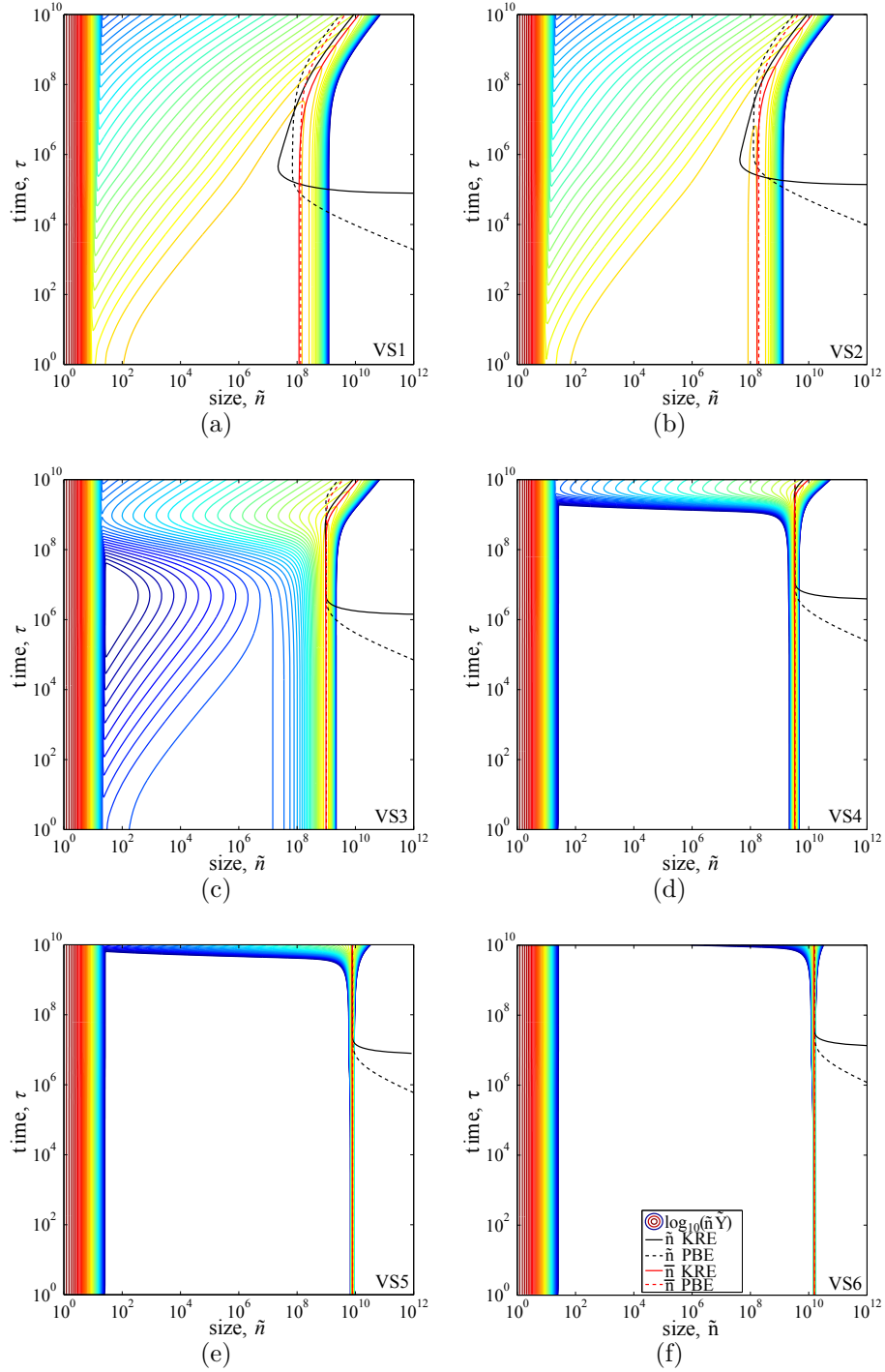


Figure 10: Seeded simulations at varying supersaturation: complete evolution of the volume weighted particle size distributions (contour plots), critical size (black lines) and mean particle size (red lines). Results from the KRE model are shown as solid lines and results from the PBE model are shown as dashed lines. The color scale for the contour lines is the same as used in Figure 2. The mean size of the seeded particles increases from VS1 to VS6, i.e., from (a) to (f). See Table 3 for details of the parameters used in these simulations.

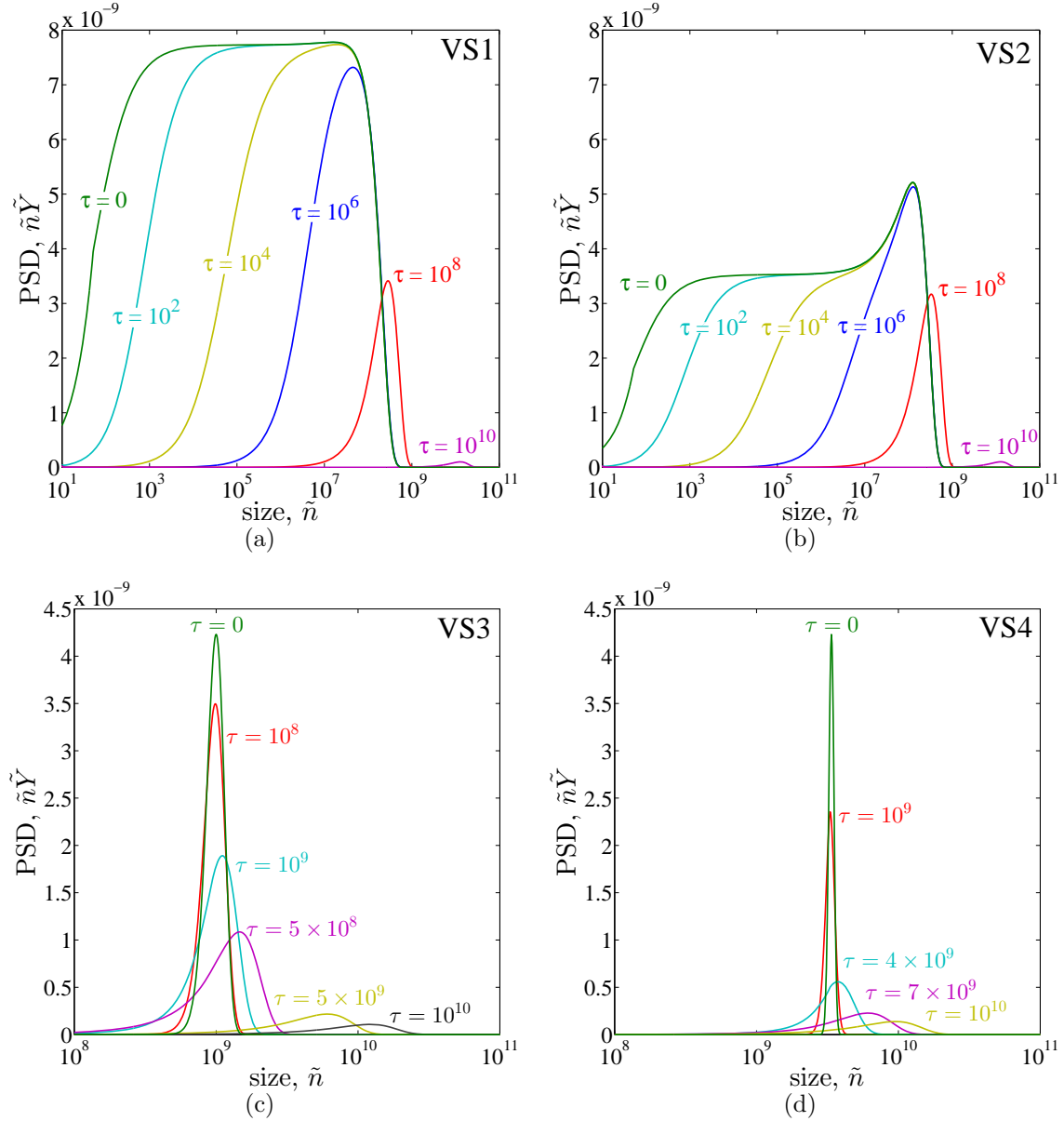


Figure 11: Seeded simulations at varying supersaturation: PSDs at selected times for simulations VS1-4. The mean size of the seeded particles increases from VS1 to VS4, i.e., from (a) to (d). See Table 3 for details of the parameters used in these simulations.

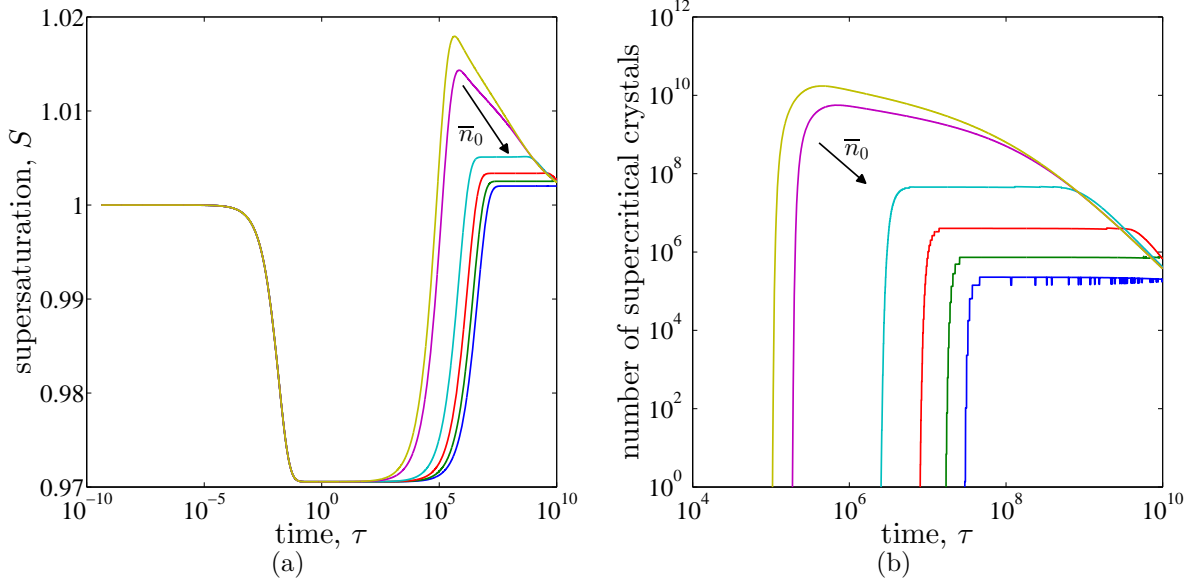


Figure 12: Seeded simulations at varying supersaturation: integral properties of the simulations; (a) evolution of supersaturation, (b) evolution of number of supercritical crystals.

Table 4: Overview of unseeded simulations at constant supersaturation (a:  $S = 1.5, \dots, n$ :  $S = 10$ )

ID	$\alpha$	$S_0$
VU1a-n	3	1.5–10
VU2a-n	4	1.5–10
VU3a-n	5	1.5–10
VU4a-n	6	1.5–10
VU5a-n	7	1.5–10
VU6a-n	8	1.5–10

504 grow before they finally undergo Ostwald ripening. By varying the key simulation parameters,  
505 i.e., the initial supersaturation and the capillary length, it is demonstrated that the KRE can  
506 not only model the entirety of this process but is indeed able to do so under a wide range of  
507 operating conditions. The parameters used in the simulations are reported in Table 4. This  
508 type of simulations cannot be performed using a classical PBE model and hence no direct  
509 comparison is possible. However, we will interpret the results in two ways:

- 510 • by using the complete evolution of the PSDs and
- 511 • by introducing characteristic times that allow us to identify dominating mechanisms at  
512 a specific time during the simulations.

513 In a first step, we focus on a single simulation and use both approaches to explain the evolution  
514 of the PSD in detail. Later on in this section, a comparative assessment of a larger set of  
515 simulations will be presented. Let us therefore consider a simulation at  $\alpha = 4$  and an initial  
516 supersaturation  $S_0 = 4$  for which the evolution of the volume weighted PSD and the critical  
517 size is illustrated in Figure 13 in the form of a contour plot, while we report the evolution of  
518 the supersaturation and the number of supercritical crystals in Figure 14(a) and Figure 14(b),  
519 respectively. Note that on Figure 13, as before, contour lines in red represent the largest  
520 values of the PSD, whereas those in blue the lowest, with the transition from red to blue given  
521 by the yellow and green hues, where the color scale is distributed logarithmically, so that it  
522 spans 25 orders of magnitude from  $10^{-24}$  to 10; note also the logarithmic scales used for both  
523 time and particle size. In Figure 14(b) the number of supercritical crystals is not smooth  
524 because of the discretized nature of our numerical solution to the kinetic rate equations.  
525 Finally, it should be noted that the number of solute molecules per suspension volume (i.e.,  
526  $Z_1$ ) is massive, so that the contour lines in the very small size range will always be shown in  
527 red color, even when the supersaturation has almost been depleted at the end of the process.  
528 To highlight this fact, we have reported  $Z_1$  in a separate curve in Figure 14(b) and have  
529 explicitly written the number of molecules at the plateau values of the supersaturation (cf.

530 Figure 14(a)) on top of this curve.

531 Analyzing the contour lines in Figure 13, we first see a “relaxation” process, i.e., the rapid  
532 formation of subcritical clusters (on the left side of the critical size). The formation of these  
533 clusters consumes a small amount of supersaturation (cf. Figure 14(a)), but no supercritical  
534 crystals have been formed yet. With increasing time the subcritical clusters grow and a  
535 small number of supercritical crystals are formed around  $\tau = 1$  (i.e., slightly after the first  
536 contour lines cross the critical size). We define the formation of the first supercritical crystal  
537 as the nucleation time,  $\tau_{\text{nuc}}$ , which shall be one of our two characteristic process times. The  
538 nucleation time marks the boundary between the relaxation phase (marked as **I** in Figure 14)  
539 and the nucleation and crystal growth phase (marked with **II** in Figure 14). Directly following  
540 the formation of the first supercritical crystal, nucleation is the dominant process (from  $\tau = 1$   
541 until  $\tau \approx 10^3$ ) and many more nuclei are formed as can be seen in Figure 14(b). However,  
542 the number of supercritical crystals reaches a plateau at  $\tau \approx 10^3$ , while the supersaturation  
543 is sharply decreasing from  $\tau \approx 10^3$  to  $\tau \approx 10^4$ . This is due to crystal growth that consumes  
544 a large number of solute molecules in this phase. The growth process can also clearly be  
545 identified by the significant increase in the average size of the supercritical crystals that can  
546 either be seen from the contour lines of the distribution, cf. Figure 13, or in Figure 14(b)  
547 where the mean size of the supercritical crystals is reported directly. Note that the growth  
548 rate used in this work (Eq. (13)) and the sharp decrease in supersaturation lead to a focusing  
549 of the size distribution that ends in a bimodal distribution consisting of subcritical clusters  
550 and supercritical crystals that are rather narrowly distributed. At the end of the crystal  
551 growth period, the supersaturation reaches another plateau and the number of supercritical  
552 crystals is at a maximum. We define this point, i.e., where the number of supercritical crystals  
553 is maximal, as the ripening time,  $\tau_{\text{rip}}$ , which signifies the end of the nucleation and crystal  
554 growth phase and the start of the process phase where Ostwald ripening becomes (potentially)  
555 important (marked with **III** in Figure 14). From this point onwards, the evolution of the  
556 process follows the behavior of the simulations presented in Section 3.2.1: a stationary period

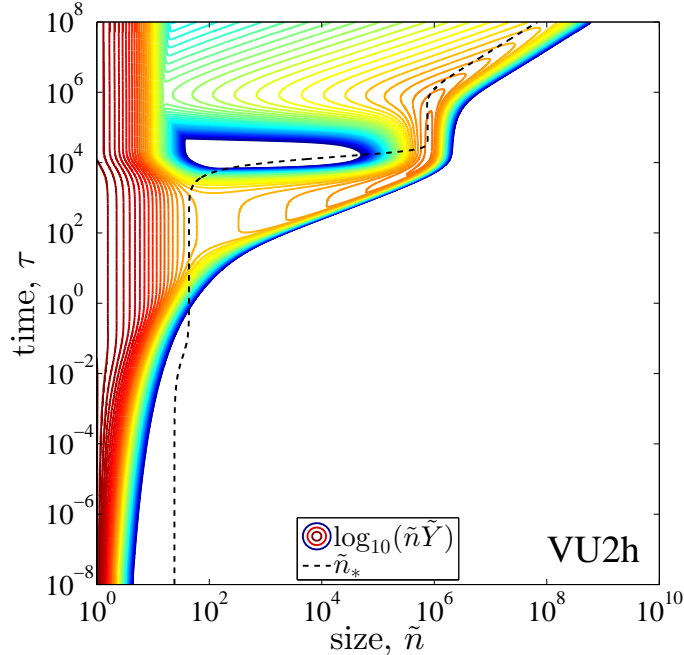


Figure 13: Unseeded simulations at varying supersaturation: evolution of volume weighted PSD for simulation VU2h with dimensionless capillary length  $\alpha = 4$  and initial supersaturation  $\xi_0 = 4$ . The dashed black line represents the critical size at the supersaturation present at that time. The color scale for the contour lines is the same as used in Figure 2.

557 where the dissolution of the smaller particles in the distribution counterbalances the growth  
 558 of the larger particles is followed by a period in which the supersaturation decreases slowly  
 559 while the critical size and mean particle size increases accordingly.

560 Widening our scope now onto a larger set of simulations with  $\alpha = 4$  and initial super-  
 561 saturations  $S_0 = 1.5, 3, 5$  and  $10$ , cf. Figure 15 and Figure 16, we can investigate how the  
 562 different process phases are affected by the change in initial supersaturation. Considering  
 563 Figure 15, we see that the onset of nucleation is observed at earlier times for increasing  
 564 initial supersaturations and thus the relaxation phase is shorter, which is consistent with  
 565 experimental observations where measured induction times are shorter at higher initial su-  
 566 persaturations. Note that the simulation at the lowest initial supersaturation (depicted in  
 567 Figure 15(a)) remains in a metastable state and the formation of supercritical crystals is  
 568 not observed within the timeframe of the simulation. Comparing subfigures b) and c) to  
 569 Figure 13, one can see that precipitated particles at the end of the nucleation and growth

570 phase are smaller for higher initial supersaturations and that the ripening phase consequently  
571 starts earlier. Note that for the highest initial supersaturation  $S_0 = 10$  (Figure 15(d)) a clear  
572 identification of the different phases is difficult as the transitions between the phases are  
573 blurry and nucleation, crystal growth and Ostwald ripening are concomittant during the  
574 transitions.

575 Focusing our attention on the supersaturation profiles reported in Figure 16(a) and the  
576 number of supercritical crystals reported in Figure 16(b) for the simulations where significant  
577 Ostwald ripening can be observed ( $S_0 = 4, 5$  and  $10$ , i.e., the purple, turquoise and red lines),  
578 we can confirm our earlier observation (Section 3.2.1) that, no matter the distribution at  
579 the start of the ripening phase (i.e., the particles precipitated in the nucleation and growth  
580 phase) a consistent behavior at later stages of the simulations is observed, i.e., the rate of  
581 disappearance of supercritical crystals and the decrease in supersaturation become the same  
582 for all the simulations.

583 The dependence of the two characteristic times,  $\tau_{\text{nuc}}$  and  $\tau_{\text{rip}}$ , on the initial supersaturation  
584 and the capillary length can be shown more comprehensively using the whole simulation set  
585 in Table 4. Hence, the characteristic times are plotted in Figure 17. It should be noted that  
586 the characteristic times were only determined for simulations where the different phases of the  
587 crystallization process could be clearly separated, so as the number of simulations in Table 4  
588 is larger than the number of data points in Figure 17. One can see that both characteristic  
589 times are shorter for shorter capillary lengths and for higher initial supersaturations. This  
590 behavior is not surprising since  $\tau_{\text{nuc}}$  is directly dependent on the nucleation rate, which in  
591 turn is higher for lower capillary lengths and higher initial supersaturations. The ripening  
592 time,  $\tau_{\text{rip}}$ , decreases for higher initial supersaturations and lower capillary lengths because  
593 smaller crystals are obtained after the process phases of relaxation, nucleation and crystal  
594 growth, as shown in Figure 15.

595 This information on characteristic times, which is only accessible via the complete  
596 description of the KRE model, could in principle be used to choose the operating conditions

597 for a process in which both nucleation and ripening occur. For example, in a precipitation  
598 process it might be desirable to delay Ostwald ripening as long as possible after particle  
599 formation, i.e. prolonging the stationary phase prior to the onset of Ostwald ripening. A  
600 (qualitative) understanding of how to accomplish this can be gained by considering the ratio of  
601 the two characteristic times, i.e.,  $\tau_{\text{rip}}/\tau_{\text{nuc}}$ . One would then wish to operate the precipitation  
602 process at a large value of this ratio by choosing appropriate operating conditions,  $S_0$  and  
603  $\alpha$ . Clearly, this is a simplification of the real problem, where both physical limitations and  
604 constraints on the target PSD would need to be taken into account as well, however, the  
605 presented analysis defines a simple number that can be used to circumvent an otherwise  
606 elusive problem.

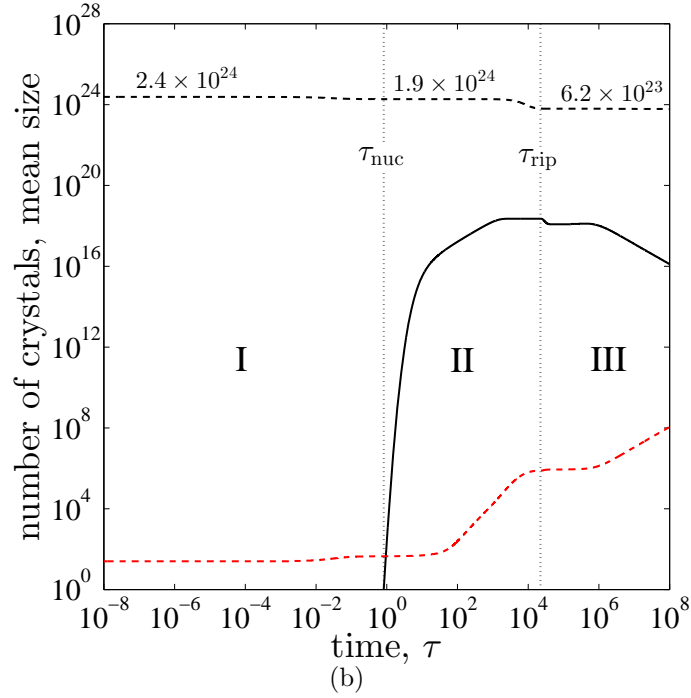
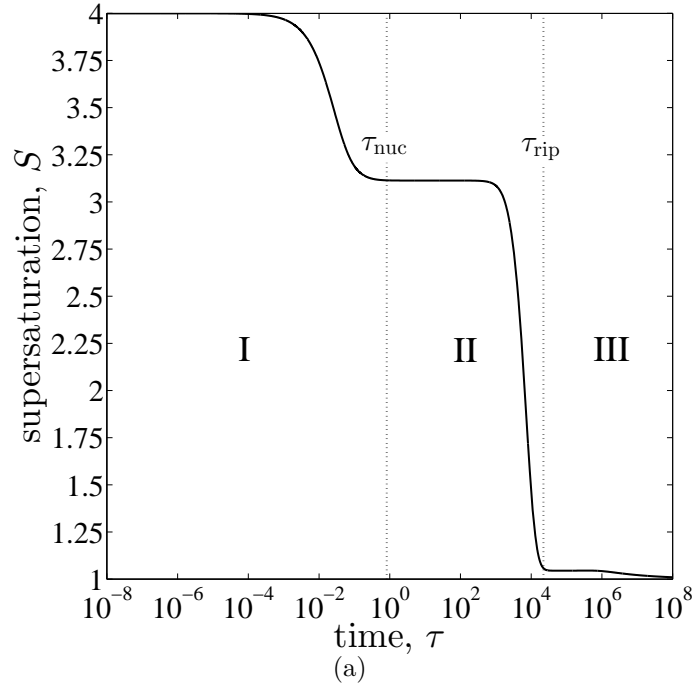


Figure 14: Unseeded simulations at varying supersaturation: integral properties of simulation VU2h with dimensionless capillary length  $\alpha = 4$  and initial supersaturation  $S_0 = 4$ ; (a) supersaturation over time, (b) number of supercritical crystals over time (solid line) and concentration of solute molecules,  $Z_1$  (black dashed line) and mean size of supercritical crystals (red dashed line). The characteristic nucleation and ripening time,  $\tau_{\text{nuc}}$  and  $\tau_{\text{rip}}$ , are indicated with black dotted lines in both subfigures.

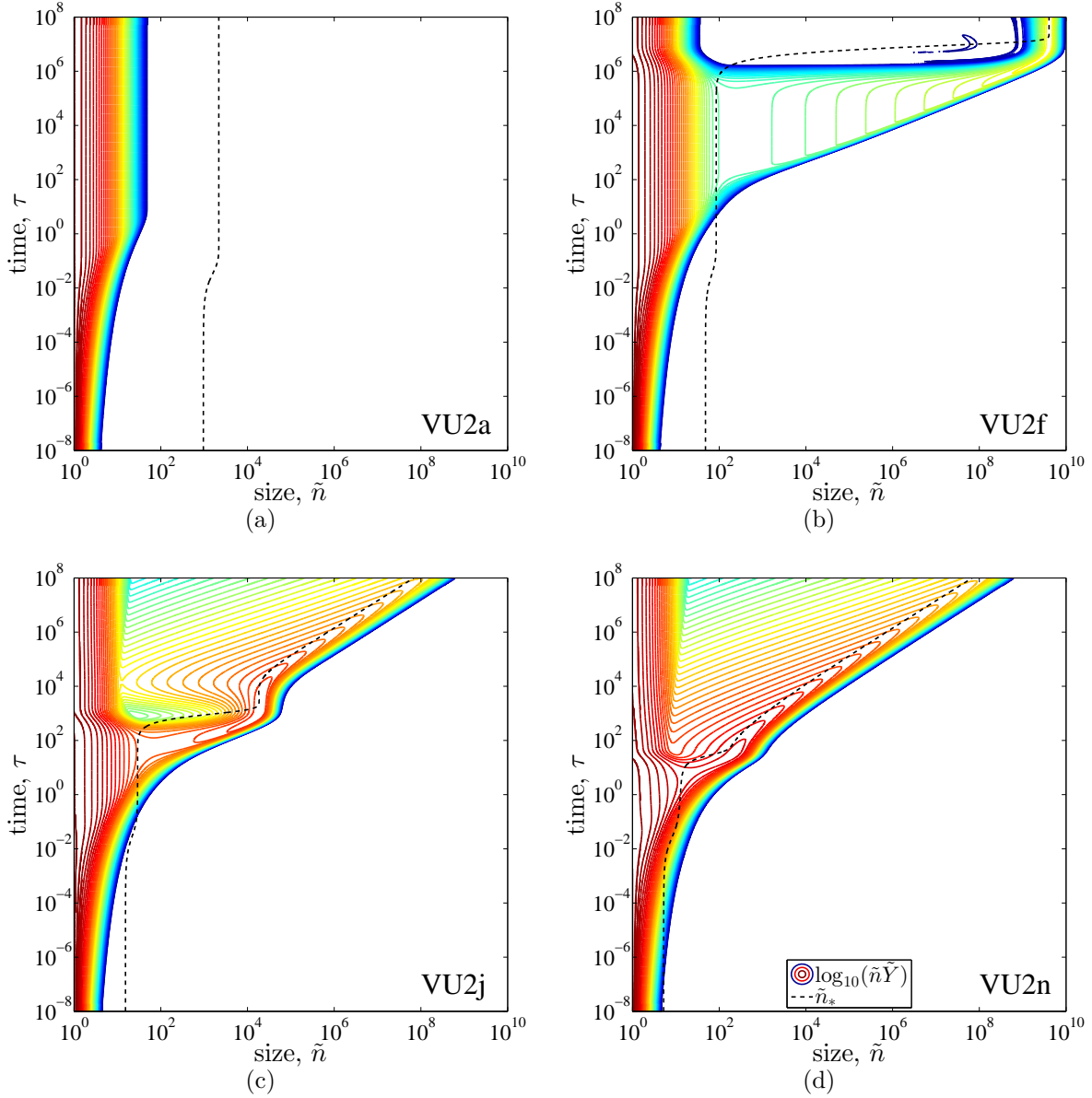


Figure 15: Unseeded simulations at varying supersaturation: evolution of volume weighted PSDs. The dashed black line represents the critical size at the supersaturation present at that time. The initial supersaturation is different in each subfigure, while the dimensionless capillary length is always  $\alpha = 4$ : (a) simulation VU2a,  $S_0 = 1.5$ , (b) simulation VU2f,  $S_0 = 3$ , (c) simulation VU2j,  $S_0 = 5$ , (d) simulation VU2n,  $S_0 = 10$ .

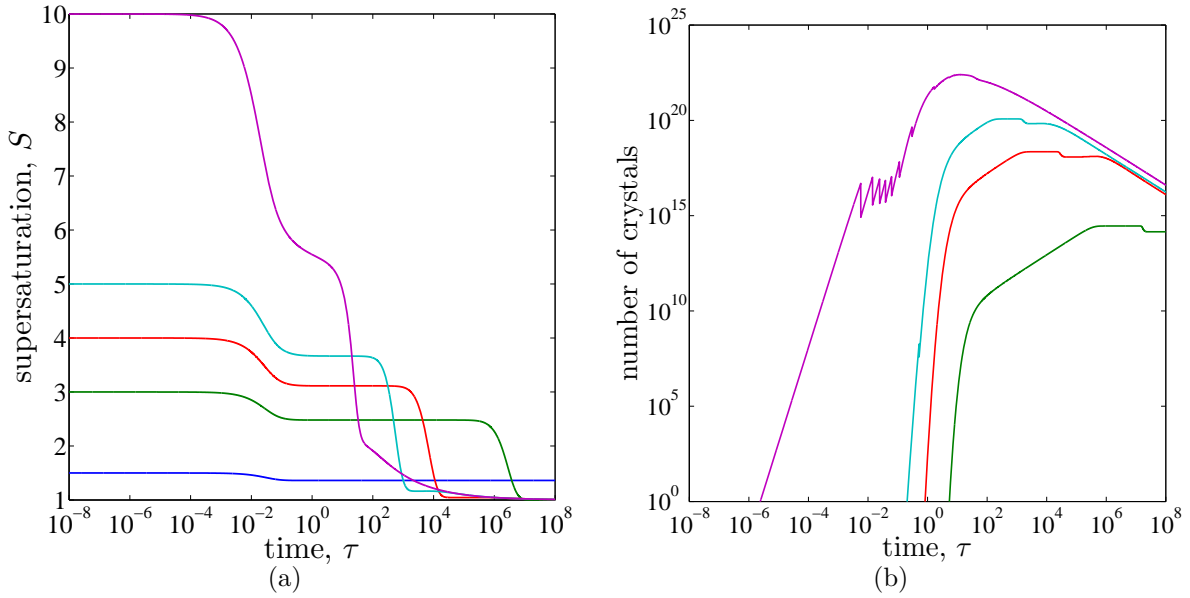


Figure 16: Unseeded simulations at varying supersaturation: integral properties of simulations VU2a, VU2f, VU2h, VU2j and VU2n with dimensionless capillary length  $\alpha = 4$  and different initial supersaturations; (a) supersaturation over time, (b) number of supercritical crystals over time. The same line color corresponds to the same simulation in both subfigures. Note that in simulation VU2a ( $S_0 = 1.5$ , blue line in subfigure a)) no supercritical crystals are formed, such that no line for this simulation is visible in subfigure b).

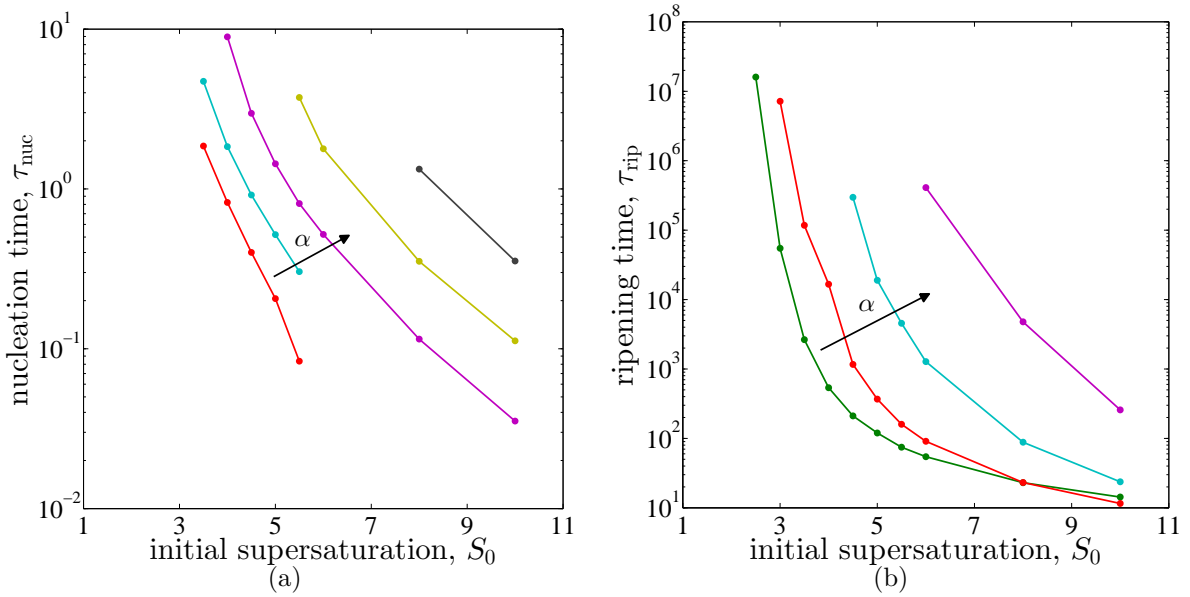


Figure 17: Unseeded simulations at varying supersaturation: characteristic times; (a) nucleation times,  $\tau_{\text{nuc}}$ , (b) ripening times,  $\tau_{\text{rip}}$ . Note that the same color has been used to represent the same dimensionless capillary length,  $\alpha$ , in the two subfigures.

## 607 4 Concluding remarks

608 In this work, two different ways of describing crystallization processes have been presented.  
609 The classical PBE model is based mainly on thermodynamic considerations, while the second  
610 type of model is based on the KRE. We have shown that the KRE model allows the simulation  
611 of all stages of a crystallization process in a single description by virtue of being self consistent  
612 and avoiding some of the strong assumptions that are used in PBE models.

613 The kinetic KRE was solved using a hybrid approach with a discrete and a continuous  
614 part, where the latter is described by a Fokker-Planck equation. The resulting model yields a  
615 good trade off between accuracy and efficiency. However, the solution of this model is still  
616 more costly than solving a PBE of similar accuracy, which can be seen as a disadvantage of  
617 the KRE model.

618 By writing both the PBE and KRE models in dimensionless form, we have identified key  
619 parameters that influence the evolution of the particle size distribution. These parameters, i.e.,  
620 initial supersaturation, initial particle size distribution and capillary length, were subsequently  
621 varied in a parameter analysis. In order to compare the PBE and KRE models, different  
622 mechanisms present in a crystallization process (nucleation, crystal growth and Ostwald  
623 ripening) were decoupled from each other by carefully choosing appropriate simulation  
624 conditions. We have confirmed for every mechanism separately that the KRE and PBE model  
625 deliver similar descriptions of the process and that the dependence of the two models on the  
626 key parameters given above is consistent. Nevertheless, the KRE model in general allows  
627 obtaining deeper insight into the behavior of both sub- and supercritical crystals.

628 A careful analysis of the results of simulations dedicated to investigate nucleation allowed  
629 us to align the parameters of the KRE and PBE models. The KRE model depends on only  
630 four parameters, namely the nominal solubility  $Z_{1,\infty} = c_\infty N_A$ , the attachment rate constant,  
631  $k$ , the constant exponent  $a$  in the attachment and detachment rates and the constant  $\alpha$ ,  
632 related to the capillary length. For the PBE model two additional (supposedly) independent  
633 parameters are typically introduced:  $K_1$  and  $K_2$ . However, our analysis shows that  $K_1$  and

634  $K_2$  can in fact be expressed as functions of the remaining parameters, indicating that the  
635 degrees of freedom in the KRE and PBE models are the same.

636 We then proceeded to use the KRE model for simulations covering the whole crystallization  
637 process. For these simulations it was thus possible to define characteristic times for the onset  
638 of nucleation and Ostwald ripening, so that the mechanism that is dominating during each  
639 phase of the crystallization process can be identified.

640 While the classical population balance equation approach is an irreplaceable tool for a  
641 wide variety of processes, we think that the unifying description of the KRE model that has  
642 been presented in this paper has conceptual and practical merits for certain applications.  
643 From a conceptual point of view, we consider the mechanisms of nucleation, crystal growth  
644 and Ostwald ripening as different aspects of the same fundamental driving force (the difference  
645 in chemical potential) since they all involve the transfer of solute molecules from a disordered,  
646 liquid phase to an ordered crystalline phase. Consequently, the mechanisms should also be  
647 described in a consistent fashion. It is our strong belief that such a unifying, continuous  
648 description of these mechanisms, without artificially decoupling them, can be achieved by  
649 implementing and solving the KRE model.

650 From a practical perspective, the way the KRE model has been formulated allows for  
651 the accurate description of crystals below the critical size also during process stages where  
652 nucleation is present (or even dominating). In the light of recent studies that have shown  
653 that agglomeration of subcritical crystals might be an important aspect in nucleation,<sup>47</sup> the  
654 possibility to model these effects for the subcritical crystals is an important feature. Although  
655 not investigated in this work, such a mechanism could be implemented in a model based on  
656 the kinetic rate equations, while an implementation in a classical PBE model that describes  
657 nucleation to occur directly at the critical size would only be reflected in a correction of  
658 the nucleation rate (i.e., it would be increased), which is an unsatisfying oversimplification  
659 of the underlying physics. Finally, we have presented a possible pathway for how KRE  
660 simulations can yield an enhanced understanding regarding the choice of operating conditions

661 for a particular process type.

662 **Supporting Information Available**

663 Derivation of size-dependent solubility and critical size, dimensionless versions of key equations  
664 in the PBE and KRE model, numerical solution scheme of the Fokker-Planck equation,  
665 additional simulations of unseeded processes at varying supersaturation. This material is  
666 available free of charge via the Internet at <http://pubs.acs.org/>.

# Notation

$a$	exponent in the crystal growth rate regarding $\tilde{n}$ dependence	[-]
$A_n$	crystal consisting of $n$ molecules	[-]
$b$	exponent in the crystal growth rate regarding concentration dependence	[-]
$c$	solution concentration	[mol m <sup>-3</sup> ]
$c_\infty$	bulk solubility	[mol m <sup>-3</sup> ]
$c_*(n)$	solubility of a crystal containing $n$ molecules	[mol m <sup>-3</sup> ]
$f(\tilde{n}, t)$	number-based particle size distribution	[m <sup>-3</sup> ]
$g(\tilde{n})$	rate constant for attachment of a single molecule from a crystal of size $n$	[m <sup>3</sup> s <sup>-1</sup> ]
$g(n, j)$	rate constant for attachment between crystals of size $n$ and $j$	[m <sup>3</sup> s <sup>-1</sup> ]
$G$	Gibbs free energy	[J]
$h(\tilde{n})$	rate constant for the detachment of a single molecule from crystal of size $n$	[s <sup>-1</sup> ]
$h(n, j)$	rate constant for the detachment of a crystal with size $j$ from a crystal with size $n$	[s <sup>-1</sup> ]
$H(\tilde{n})$	dispersion coefficient in the Fokker-Planck equation	[s <sup>-1</sup> ]
$J$	nucleation rate	[m <sup>-3</sup> s <sup>-1</sup> ]
$k$	prefactor in the growth rate expression (Eq. (13))	[m <sup>3b</sup> s <sup>-1</sup> ]
$K_1$	prefactor in the nucleation rate expression (Eq. (4))	[m <sup>-3</sup> s <sup>-1</sup> ]
$K_2$	constant in the exponential part of the nucleation rate expression (Eq. (4))	[-]
$n$	crystal size in number of molecules	[-]
$\tilde{n}$	continuous crystal size in number of molecules	[-]
$\tilde{n}_*$	critical size	[-]
$\bar{n}$	mean particle size	[-]
$n_0$	mean of seed distribution	[-]
$N$	maximum particle size included in the discrete part of the multi-scale model	[-]
$N_A$	Avogadro constant	[mol <sup>-1</sup> ]
$R$	ideal gas constant	[J mol <sup>-1</sup> K <sup>-1</sup> ]
$S$	supersaturation	[-]
$S_0$	initial supersaturation	[-]
$t$	time	[s]
$t_0$	characteristic time	[s]
$T$	temperature	[K]
$v(\tilde{n})$	crystal growth rate	[s <sup>-1</sup> ]
$X_n$	dimensionless concentration of crystals of size $n$ under stationary conditions	[-]
$Y_n$	dimensionless concentration of crystals of size $n$	[-]

$\tilde{Y}(\tilde{n})$	dimensionless number density distribution in continuous form	[-]
$Z_n$	concentration of crystals of size $n$	[m <sup>-3</sup> ]
$Z_1^*(n)$	solubility of a crystal containing $n$ molecules	[m <sup>-3</sup> ]
$Z_{1,\infty}$	bulk solubility	[m <sup>-3</sup> ]
$\tilde{Z}(\tilde{n})$	number density distribution of crystals in continuous form	[m <sup>-3</sup> ]
$\alpha$	dimensionless capillary length	[-]
$\delta$	Dirac delta function	[-]
$\eta_n$	dimensionless rate constant for the detachment of a single molecule from crystal of size $n$	[-]
$\mu_j$	$j$ -th moment of $\tilde{Y}$	[-]
$\xi_n$	dimensionless rate constant for the detachment of a single molecule from a crystal of size $n$	[-]
$\phi$	instantaneous dimensionless nucleation rate	[-]
$\bar{\phi}$	stationary dimensionless nucleation rate	[-]
$\sigma_0$	standard deviation of seed distribution	[-]
$\tau$	dimensionless time	[-]
$\tau_{\text{lag}}$	lag time	[-]
$\tau_{\text{nuc}}$	characteristic nucleation time	[-]
$\tau_{\text{rip}}$	characteristic ripening time	[-]
$\psi$	initial hold up ratio	[-]

## References

- 669 (1) Ostwald, W. *Z. Phys. Chem.* **1900**, *34*, 495–503.
- 670 (2) Voorhees, P. W. *J. Stat. Phys.* **1985**, *38*, 231–252.
- 671 (3) Randolph, A. D.; Larson, M. A., *Theory of particulate processes : analysis and techniques*  
672 *of continuous crystallization*; Academic Press: New York, 1971.
- 673 (4) Leblanc, S. E.; Fogler, H. S. *AIChE J.* **1987**, *33*, 54–63.
- 674 (5) Ramkrishna, D. *Population Balances: Theory and Applications to Particulate Systems*  
675 *in Engineering*; Academic Press: San Diego, CA, 2000.
- 676 (6) Kashchiev, D. *Nucleation*; Butterworth-Heinemann: Oxford, U.K., 2000.
- 677 (7) Mersmann, A., *Crystallization Technology Handbook*, 2nd ed.; Marcel Dekker: New  
678 York, 2001.
- 679 (8) Mullin, J. W., *Crystallization*, 4th ed.; Butterworth-Heinemann: Oxford, U.K., 2001.
- 680 (9) Volmer, M.; Weber, A. *Z. Phys. Chem.* **1926**, *119*, 277–301.
- 681 (10) Farkas, L. *Z. Phys. Chem.* **1927**, *125*, 236–242.
- 682 (11) Lindenberg, C.; Mazzotti, M. *J. Cryst. Growth* **2009**, *311*, 1178 – 1184.
- 683 (12) Lindenberg, C.; Mazzotti, M. *AIChE Journal* **2011**, *57*, 942–950.
- 684 (13) Hulburt, H. M.; Katz, S. *Chem. Eng. Sci.* **1964**, *19*, 555–574.
- 685 (14) Tavare, N.; Garside, J. *Chem. Eng. Res. Des.* **1986**, *64*, 109–118.
- 686 (15) Randolph, A. D. *Ind. Eng. Chem. Fund.* **1969**, *8*, 58–63.
- 687 (16) Kostoglou, M.; Dovas, S.; Karabelas, A. J. *Chem. Eng. Sci.* **1997**, *52*, 1285–1299.
- 688 (17) Zauner, R.; Jones, A. G. *Chem. Eng. Sci.* **2000**, *55*, 4219–4232.
- 689 (18) Kougoulos, E.; Jones, A. G.; Wood-Kaczmar, M. W. *J. Cryst. Growth* **2005**, *273*,  
690 520–528.
- 691 (19) Lindenberg, C.; Schöll, J.; Vicum, L.; Mazzotti, M.; Brozio, J. *Cryst. Growth Des.* **2008**,  
692 *8*, 224–237.
- 693 (20) Lifshitz, I. M.; Slyozov, V. V. *J. Phys. Chem. Solids* **1961**, *19*, 35–50.
- 694 (21) Wagner, C. *Z. Elektrochem.* **1961**, *65*, 581–591.
- 695 (22) Tavare, N. S. *AIChE J.* **1987**, *33*, 152–156.
- 696 (23) Ståhl, M.; Åslund, B.; Rasmuson, Å. C. *Ind. Eng. Chem. Res.* **2004**, *43*, 6694–6702
- 697

- 698 (24) Hoang, T. K. N.; Deriemaeker, L.; Finsy, R. *Langmuir* **2004**, *20*, 8966–8969.
- 699 (25) Liu, Y.; Kathan, K.; Saad, W.; Prud’homme, R.K. *Phys. Rev. Lett.*, **2007**, *98*, 36102.
- 700 (26) Iggländ, M.; Mazzotti, M. *Cryst. Growth Des.* **2012**, *12*, 1489–1500.
- 701 (27) Ozkan, G.; Ortoleva, P. *J. Chem. Phys.* **2000**, *112*, 10510–10525.
- 702 (28) Rempel, J. Y.; Bawendi, M. G.; Jensen, K. F. *J. Am. Chem. Soc.* **2009**, *131*, 4479–4489.
- 703 (29) Amal, Y.; Pinto, M. C. *Discret. Contin. Dyn. S. B* **2010**, *13*, 517–535.
- 704 (30) Madras, G.; McCoy, B. J. *Chem. Eng. Sci.* **2002**, *57*, 3809–3818.
- 705 (31) Noguera, C.; Fritz, B.; Clément, A.; Baronnet, A. *J. Cryst. Growth* **2006**, *297*, 180–186.
- 706 (32) Noguera, C.; Fritz, B.; Clément, A.; Baronnet, A. *J. Cryst. Growth* **2006**, *297*, 187–198.
- 707 (33) Uwaha, M.; Koyama, K. *J. Cryst. Growth* **2010**, *312*, 1046–1054.
- 708 (34) Dubrovskii, V. G.; Nazarenko, M. V. *J. Chem. Phys.* **2010**, *132*, 114507.
- 709 (35) Dubrovskii, V. G.; Nazarenko, M. V. *J. Chem. Phys.* **2010**, *132*, 114508.
- 710 (36) Dubrovskii, V. G.; Kazansky, M. A., Nazarenko, M. V.; Adzhemyan, L. T. *J. Chem.*  
711 *Phys.* **2011**, *134*, 094507.
- 712 (37) Hounslow, M.J. *AIChE J.* **1990**, *36*, 106–116.
- 713 (38) Kumar, S.; Ramkrishna, D. *Chem. Eng. Sci.* **1997**, *52*, 4659–4679.
- 714 (39) Qamar, S.; Elsner, M.P.; Angelov, I.A.; Warnecke, G.; Seidel-Morgenstern, A. *Comput.*  
715 *Chem. Eng.* **2006**, *30*, 1119–1131.
- 716 (40) Rigopoulos, S. *Prog. Energy Combust. Sci.* **2010**, *36*, 412–443.
- 717 (41) Ono, T.; Kramer, H. J. M.; ter Horst, J. H.; Jansens, P. J. *Cryst. Growth Des.* **2004**, *4*,  
718 1161–1167.
- 719 (42) Vetter, T.; Mazzotti, M.; Brozio, J. *Cryst. Growth Des.* **2011**, *11*, 3813–3821.
- 720 (43) Gherras, N.; Févotte, G. *AIChE J.* **2012**, *58*, 2650–2664.
- 721 (44) Stroock, D. W. *An introduction to Markov processes*; Springer: Berlin, Germany, 2005.
- 722 (45) Davey, R.J.; Garside, J. *From Molecules to Crystallizers: An Introduction to Crystal-*  
723 *lization*; Oxford University Press: Oxford, U.K., 2000.
- 724 (46) Kashchiev, D.; van Rosmalen, G. M. *Cryst. Res. Technol.* **2003**, *38*, 555–574.
- 725 (47) Yuk J. M.; Park, J.; Ercius, P.; Kim, K.; Hellebusch, D. J.; Crommie, M. F.; Lee, J. Y.;  
726 Zettl, A.; Alivisatos, A. P. *Science* **2012**, *336*, 61–64.

- 727 (48) Kashchiev, D. *Cryst. Res. Technol.* **1984**, *19*, 1413–1423.
- 728 (49) Ohara, M.; Reid, R. C. *Modeling Crystal Growth Rates from Solution*; Prentice Hall:  
729 Upper Saddle River, NJ, 1973.
- 730 (50) Shampine, L. F.; Reichelt, M. W. *SIAM J. Sci. Comput.* **1997**, *18*, 1–22.
- 731 (51) Shampine, L. F.; Reichelt, M. W.; Kierzenka, J. A. *SIAM Rev.* **1999**, *41*, 538–552.
- 732 (52) Chang, J. S.; Cooper, G. J. *J. Comput. Phys.* **1970**, *6*, 1–16.
- 733 (53) Rempel, J. Y., *Insights into Formation of Semiconductor Nanocrystals: From First*  
734 *Principles Calculations to Kinetic Models of Nucleation and Growth*, MIT: Cambridge,  
735 2008.
- 736 (54) Rhee, H.-K.; Aris, R.; Amundson, N. R., *First-order Partial Differential Equations:*  
737 *Theory and application of single equations*; Dover Publications: Mineola, NY, 1986.
- 738 (55) Hänggi, P.; Grabert, H.; Talkner, P.; Thomas, H. *Phys. Rev. A* **1984**, *29*, 371–378.
- 739 (56) Shizgal, B.; Barrett, J. C. *J. Chem. Phys.* **1989**, *91*, 6505–6518.
- 740 (57) Wu, D. T. *Solid State Phys.* **1996**, *50*, 37–187.

741 **For Table of Contents Use Only**

742 **Title:** Modeling Nucleation, Growth and Ostwald Ripening in Crystallization Processes: A  
743 Comparison Between Population Balance and Kinetic Rate Equation

744 **Authors:** Thomas Vetter, Martin Iggländ, David R. Ochsenein, Flurin S. Hänseler, and  
745 Marco Mazzotti

746 **Synopsis:** Nucleation, crystal growth and Ostwald ripening are simulated using population  
747 balance equation and kinetic rate equation models. We show that only models based on kinetic  
748 rate equations can describe the full crystallization process in a physically consistent way. We  
749 identify key parameters that influence the kinetics of the above-mentioned crystallization  
750 mechanisms and present a thorough parameter study.

